Fluid Dyn. Res. **44** (2012) 065506 (38pp) doi:10.1088/0169-5983/44/6/065506

Helical solutions of the bidirectional vortex in a cylindrical cyclone: Beltramian and Trkalian motions

Joseph Majdalani

Department of Mechanical, Aerospace and Biomedical Engineering, University of Tennessee Space Institute (UTSI), 411 B. H. Goethert Parkway, Tullahoma, TN 37388, USA

E-mail: joe.majdalani@gmail.com

Received 16 October 2011, in final form 25 September 2012
Published 31 October 2012
Online at stacks.iop.org/FDR/44/065506

Communicated by M Funakoshi

Abstract
In this work, two families of helical motions are investigated as prospective candidates for describing the bidirectional vortex field in a right-cylindrical chamber. These basic solutions are relevant to cyclone separators and to idealized representations of vortex-fired liquid and hybrid rocket engines in which bidirectional vortex motion is established. To begin, the bulk fluid motion is taken to be isentropic along streamlines, with no concern for reactions, heat transfer, viscosity, compressibility or unsteadiness. Then using the Bragg–Hawthorne equation for steady, inviscid, axisymmetric motion, two families of Euler solutions are derived. Among the characteristics of the newly developed solutions one may note the axial dependence of the swirl velocity, the Trkalian and Beltramian types of the helical motions, the sensitivity of the solutions to the outlet radius, the alternate locations of the mantle, and the increased axial and radial velocity magnitudes, including the rate of mass transfer across the mantle, for which explicit approximations are obtained. Our results are compared to an existing, complex lamellar model of the bidirectional vortex in which the swirl velocity reduces to a free vortex. In this vein, we find the strictly Beltramian flows to share virtually identical pressure variations and radial pressure gradients with those associated with the complex lamellar motion. Furthermore, both families warrant an asymptotic treatment to overcome their endpoint limitations caused by their omission of viscous stresses. From a broader perspective, the work delineates a logical framework through which self-similar, axisymmetric solutions to bidirectional and multidirectional vortex motions may be pursued. It also illustrates the manner through which different formulations may be arrived at depending on the types of wall boundary conditions. For example, both the slip condition at the sidewall and the inlet flow pattern at the headwall may be enforced or relaxed.

0169-5983/12/065506+38$33.00

1. Introduction

Cyclonic motions pertain to a number of vortex-fired engine technologies including such devices as the Vortex Hybrid Engine introduced by Gloyer *et al* (1993), the Vortex Injection Hybrid Rocket Engine (VIHRE) conceived by Knuth *et al* (1996), the Vortex Combustion Cold-Wall Chamber (VCCWC) developed by Chiaverini *et al* (2003), and the Reverse Vortex Combustor spawned by Matveev *et al* (2007). In addition to their propulsive function, these fascinating swirl-induced patterns are inherently connected to meteorological phenomena such as tornadoes, hurricanes (i.e. tropical cyclones), dust devils, and typhoons (Penner 1972); astrophysical activities of cosmic spirals, galactic pinwheels, and helical trajectories of celestial bodies (Königl 1986, Kirshner 2004); and industrial processes involving cyclonic separators, combustors, and furnaces (Reydon and Gauvin 1981).

For the cylindrical cyclone, some of the earliest laboratory investigations point to ter Linden (1949) whose efforts to characterize dust separation efficiency were quickly succeeded by the classical experiments on hydraulic and gas cyclones performed by Kelsall (1952) and Smith (1962a, 1962b). These fundamental experiments may have been first to suggest the existence of forced, rather than free vortex behaviour in the core region of a cyclone. Other theoretical studies of hydraulic cyclones emerged but these were chiefly based on semi-empirical methods (Fontein and Dijksman 1953). Among them stood the Polhausen technique that was introduced in the context of a conical cyclone and later traded by Bloor and Ingham (1973, 1987) for a more detailed differential approach.

With the widespread use of computational resources, the Bloor–Ingham model was followed by a period in which emphasis was shifted to two- and three-dimensional simulations of cyclonic devices. Several experimental and numerical investigations have since been carried out including those by Hsieh and Rajamani (1991), Hoekstra *et al* (1998), Hoekstra *et al* (1999), Derksen and van den Akker (2000), Fang *et al* (2003), Rom *et al* (2004), Murray *et al* (2004), Hu *et al* (2005), Zhiping *et al* (2008) and Molina *et al* (2008). In retrospect, an extensive survey on this subject by Cortes and Gil (2007) confirms that most realistic mean flow models of cyclone separators remain empirical in nature. As for the numerical simulations carried out so far, most seem to be turbulence-model dependent and, in their own way, limited in their ability to provide universal predictions, especially in the case of multi-directional flows.

Given the shortage of purely analytical models of axisymmetric cyclonic flows (e.g. Vatistas *et al* 2005), an Eulerian based solution was developed by Vyas and Majdalani (2006) for a right-cylindrical VCCWC chamber model. Although their effort only produced a simple solution for the problem at hand, it set the pace for a laminar boundary layer treatment of the viscous core and sidewall region by Majdalani and Chiaverini (2009). In the interim, the extension to the hybrid vortex configuration was conceived and carried out by Majdalani (2007). As for the sidewall boundary layers, they were reconstructed in the tangential direction and extended to the axial and radial orientations by Batterson and Majdalani (2010).

Despite these incremental advancements, the analytical treatment of the core region remained, effectively, incomplete. This was especially true at high Reynolds numbers for which the aforementioned studies overpredicted the maximum swirl velocity. To partly address this issue, Maicke and Majdalani (2009) applied a turbulence-based, constant shear stress model to the core region from which they extracted a piecewise, Rankine-like approximation for the swirl velocity. In the same work, it was shown that the use of a higher effective turbulent eddy viscosity in the calculation of the vortex Reynolds number would lead to fair agreement with experimental measurements.

Along similar lines, realizing the need to explore other potential flow candidates to this problem, Majdalani and Rienstra (2007) turned their attention to the general vorticity equation in spherical coordinates. This effort enabled them to identify uniform, linear and nonlinear classes of Eulerian solutions for problems with constant angular momentum. These were classified according to the relation established between their tangential mean flow vorticity ω_θ and their stream function ψ. Their type I representation displayed uniform vorticity and reproduced, in one case, the potential flow past a sphere, namely, the external portion of Hill's spherical vortex (Hill 1894). Their type II solution relied on a linear relation $\omega \sim \psi$ and reproduced, in one situation, the bidirectional vortex in a cylindrical chamber. Finally, their type III considered nonlinear relations of the form $\omega \sim \psi^q$; $q \neq (0, 1)$. These representations gave rise to interesting flow patterns that could be computed numerically for $q \neq (-3, 0, 1)$ or exacted analytically for $q = -3$.

In seeking additional types of solutions that are recoverable from the spherical Bragg–Hawthorne equation (BHE; Bragg and Hawthorne 1950), Barber and Majdalani (2009) revisited the conical cyclonic flow problem that was first examined by Bloor and Ingham (1987). Their analysis led to a self-similar, verifiable solution that remained independent of the cone's finite body length. It also gave rise to explicit approximations of several flow attributes such as the mantle location, maximum chamber velocities, crossflow velocities, and both pressure and vorticity distributions. Finally, it permitted the identification of the basic forms of the angular momentum relation to the stream function and to the procedural steps required to (i) account for the spatial variance of the swirl velocity and (ii) capture the effects of a specific injection flow pattern. In this article, a similar procedure is implemented in the context of axisymmetric cyclonic motion in a right-cylindrical chamber. This effort will give rise to multiple helical solutions of the Beltramian and Trkalian types, depending on the sidewall boundary conditions imposed on the tangential velocity. Our analysis will be carried out in the context of a right-cylindrical chamber first without and then with allowance for sidewall injection. The latter will enable us to model the basic flow in the so-called VIHRE.

2. Problem formulation

2.1. Cylindrical Bragg–Hawthorne equation

The cyclonic motion in a confined cylinder such as the one depicted in figure 1(a) was previously explored using the vorticity-stream function approach by Vyas and Majdalani (2006), Majdalani and Rienstra (2007), and, more recently, by Maicke and Majdalani (2009). The present framework is markedly different and begins by considering the BHE given by Batchelor (1967); accordingly, the analysis may be initiated from

$$\frac{\partial^2\psi}{\partial r^2} - \frac{1}{r}\frac{\partial\psi}{\partial r} + \frac{\partial^2\psi}{\partial z^2} = r^2\frac{\mathrm{d}H}{\mathrm{d}\psi} - B\frac{\mathrm{d}B}{\mathrm{d}\psi}, \tag{2.1}$$

where $B = ru_\theta$ and $H = p/\rho + \boldsymbol{u}\cdot\boldsymbol{u}/2$ denote the tangential angular momentum and the total pressure head, respectively. Everywhere, the nomenclature and conditions used by Majdalani and Rienstra (2007) are adhered to as illustrated in figure 1(b).

It may be instructive to note that (2.1) may be linearized by choosing conditions leading to a simple right-hand-side that returns either a constant, as in the case of Bloor and Ingham (1987), or a linear function of ψ, as in the case of Vyas and Majdalani (2006). Such conditions

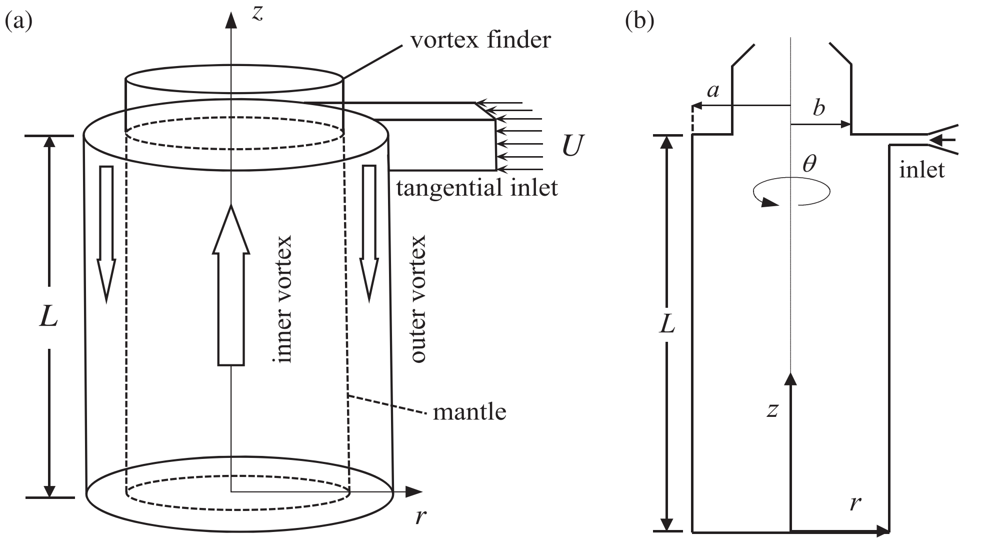

Figure 1. Schematic of a cylindrical cyclonic chamber showing (a) separate vortex regions and (b) coordinate system used.

arise when B is either constant or

$$\begin{cases} B\dfrac{\mathrm{d}B}{\mathrm{d}\psi} = \text{const}, \\[2ex] B\dfrac{\mathrm{d}B}{\mathrm{d}\psi} \sim \psi, \end{cases} \quad \begin{cases} B = \sqrt{B_0\psi + B_1}, & (a) \\[2ex] B = \sqrt{B_0\psi^2 + B_1}. & (b) \end{cases} \tag{2.2}$$

As for H, it has to be either constant or

$$\begin{cases} \dfrac{\mathrm{d}H}{\mathrm{d}\psi} = \text{const}, \\[2ex] \dfrac{\mathrm{d}H}{\mathrm{d}\psi} \sim \psi, \end{cases} \quad \begin{cases} H = H_0\psi, & (a) \\[2ex] H = H_0\psi^2 + H_1. & (b) \end{cases} \tag{2.3}$$

For example, in the development of the complex lamellar predecessor, Vyas and Majdalani (2006) have implicitly used $B(\psi) = 1$, $\mathrm{d}B/\mathrm{d}\psi = 0$ and $\mathrm{d}H/\mathrm{d}\psi = -C^2\psi$, to the extent of producing a linear BHE. Presently, this order will be reversed as we follow Bloor and Ingham (1987) and assume isentropic conditions that permit setting $\mathrm{d}H/\mathrm{d}\psi = 0$. This assumption leads to a slight generalization by granting the angular momentum dependence on the stream function

$$B(\psi) = ru_\theta = \sqrt{B_0\psi^2 + B_1}. \tag{2.4}$$

For simplicity, we take $B_0 = C^2$ and put

$$B\frac{\mathrm{d}B}{\mathrm{d}\psi} = C^2\psi, \tag{2.5}$$

where C^2 denotes some constant that needs to be determined from judiciously posed boundary conditions. Inserting (2.5) into the BHE, one obtains

$$\frac{\partial^2\psi}{\partial r^2}-\frac{1}{r}\frac{\partial\psi}{\partial r}+\frac{\partial^2\psi}{\partial z^2}+C^2\psi=0, \tag{2.6}$$

which resembles the equation considered by Vyas and Majdalani (2006) except for the absence of an r^2 multiplying the last member of (2.6). As usual, one may assume $\psi(r,z)=f(r)g(z)$ and transform (2.6) into

$$-\frac{\ddot{g}(z)}{g(z)}=\frac{1}{f}\left(f''-\frac{1}{r}f'+C^2f\right)=\begin{cases}0,\\ +\upsilon^2,\\ -\upsilon^2.\end{cases} \tag{2.7}$$

where primes and overdots denote differentiation with respect to r and z, respectively. At the outset, three solutions arise and these depend on the choice of the separation constant:

$$\psi(r,z)=\begin{cases} r(c_1z+c_2)\left[c_3J_1(Cr)+c_4Y_1(Cr)\right], & \upsilon=0,\\ r\left[c_1\sin(\upsilon z)+c_2\cos(\upsilon z)\right]\left[c_3J_1(r\sqrt{C^2-\upsilon^2})+c_4Y_1(r\sqrt{C^2-\upsilon^2})\right], & \upsilon^2\leqslant C^2,\\ r\left[c_1\sinh(\upsilon z)+c_2\cosh(\upsilon z)\right]\left[c_3J_1(r\sqrt{C^2+\upsilon^2})+c_4Y_1(r\sqrt{C^2+\upsilon^2}\right], & \upsilon^2>C^2.\end{cases} \tag{2.8}$$

In practice, it may be shown that the second and third solutions are equivalent, and this may be attributed to the ability of the sinh-based expression to replicate its sine-based counterpart when its separation constant υ is replaced by $\pm\mathrm{i}\upsilon$. For the bidirectional motion in a cylindrical chamber, an assortment of constraints may be imposed directly on these partial solutions, consistently with the work of Majdalani and Rienstra (2007). These are

$$\begin{cases} z=0, & u_z(r,0)=0, & \partial\psi/\partial r=0, & (a)\\ r=0, & u_r(0,z)=0, & \partial\psi/\partial z=0, & (b)\\ r=a, & u_r(a,z)=0, & \partial\psi/\partial z=0. & (c)\end{cases} \tag{2.9}$$

As for the sidewall condition on u_θ, two conditions may be systematically considered. The first enforces a zero tangential velocity at the wall, $u_\theta(a,z)=0$, whereas the second matches the outer circumferential velocity to the maximum tangential speed at entry, $u_\theta(a,z)=U$. The outcome of each of these assumptions will be evaluated below. Furthermore, the $\upsilon=0$ case will constitute our chief focus. The remaining two cases give rise to nonlinear variations in z. Their superposition over multiple values of υ leads to a more elaborate mathematical framework that will be discussed in future work. In the present analysis, only the case of a single valued υ will be considered first without and then, with sidewall injection.

2.2. Similarity conforming solutions

The first condition in (2.9) requires the vanishing of the axial velocity at the headwall or $c_2=0$. Along similar lines, one must set $c_4=0$ to suppress the unbounded behaviour of the radial velocity at the centreline. This leaves us with $\psi=\psi_0 z\,r J_1(Cr)$, where $\psi_0\equiv c_1c_3$. The third condition yields

$$J_1(C\,a) = 0, \quad C_m = \frac{\lambda_m}{a}, \quad m = 1, 2, 3, \ldots, \tag{2.10}$$

where $\lambda_m = \{3.83171, 7.01559, 10.1735, 13.3237, \ldots\}$ denote the roots of the Bessel function of the first kind. For a single turning point behaviour, one takes $C_1 = \lambda_1/a = 3.83171/a$, $\psi = \psi_0 z\, r\, J_1(\lambda_1 r/a)$ and puts

$$\boldsymbol{u} = -\psi_0 J_1\left(\lambda_1 \frac{r}{a}\right)\boldsymbol{e}_r + \frac{1}{r}\left[\psi_0^2\lambda_1^2 r^2\left(\frac{z}{a}\right)^2 J_1^2\left(\lambda_1\frac{r}{a}\right) + B_1\right]^{1/2}\boldsymbol{e}_\theta + \psi_0\frac{z}{a}\lambda_1 J_0\left(\lambda_1\frac{r}{a}\right)\boldsymbol{e}_z. \tag{2.11}$$

It may be instructive to note that, owing to (2.5), only one value of C_m may exist for a given cyclonic flow configuration. It may also be shown that, for the problem under investigation, only odd flow reversal mode numbers prove to be physical, and these correspond to $\lambda_1, \lambda_3, \ldots$ for which the axial velocity exhibits one, three, or more internal nodes.

At this juncture, the constant ψ_0 may be secured from a global mass balance. At steady state, a volumetric rate of $Q_i = U A_i$ entering the chamber must exit through the downstream opening of radius b (see figure 1(b)). This enables us to write

$$2\pi\int_0^b \boldsymbol{u}\cdot\hat{\boldsymbol{n}} r\,\mathrm{d}r = 2\pi\int_0^b u_z(r, L)\, r\,\mathrm{d}r = Q_i \tag{2.12}$$

and deduce

$$\psi_0 = \frac{Q_i}{2\pi a\beta L J_1(\lambda_1\beta)}, \tag{2.13}$$

where $\beta = b/a$ is the open fraction of the radius at $z = L$.

At this stage, one of two boundary conditions may be used for the tangential velocity. By analogy with the Taylor–Culick inviscid profile that self-satisfies no slip at the wall (Majdalani and Saad 2007), we first attempt to impose, $u_\theta(a, z) = 0$, or $B_1 = 0$. The problem simplifies considerably with the elimination of the leading r^{-1} term and the attendant singularity at the centreline. We are left with

$$u_\theta = \psi_0\lambda_1\left(\frac{z}{a}\right) J_1\left(\lambda_1\frac{r}{a}\right). \tag{2.14}$$

2.3. Normalization

Using the standard reference values introduced by Majdalani and Rienstra (2007), we put

$$\begin{cases} \bar{r} = \dfrac{r}{a}, \quad \bar{z} = \dfrac{z}{a}, \quad \bar{u}_r = \dfrac{u_r}{U}, \quad \bar{u}_\theta = \dfrac{u_\theta}{U}, \quad \bar{u}_z = \dfrac{u_z}{U}, \\ \bar{p} = \dfrac{p}{\rho U^2}, \quad \bar{\psi} = \dfrac{\psi}{U a^2}, \quad \bar{B} = \dfrac{B}{aU}, \quad \bar{Q}_i = \dfrac{Q_i}{U a^2} = \dfrac{A_i}{a^2} = \sigma^{-1}. \end{cases} \tag{2.15}$$

The normalized velocity becomes

$$\bar{\boldsymbol{u}} = -\frac{\psi_0}{U} J_1(\lambda_1\bar{r})\,\boldsymbol{e}_r + \frac{\lambda_1\psi_0}{U}\bar{z} J_1(\lambda_1\bar{r})\,\boldsymbol{e}_\theta + \frac{\lambda_1\psi_0}{U}\bar{z} J_0(\lambda_1\bar{r})\,\boldsymbol{e}_z \tag{2.16}$$

which, by way of (2.13), leads to

$$\bar{\boldsymbol{u}} = -\frac{1}{2\pi\sigma l}\frac{J_1(\lambda_1\bar{r})}{\beta J_1(\lambda_1\beta)}\boldsymbol{e}_r + \frac{1}{2\pi\sigma l}\lambda_1\bar{z}\frac{J_1(\lambda_1\bar{r})}{\beta J_1(\lambda_1\beta)}\boldsymbol{e}_\theta + \frac{1}{2\pi\sigma l}\lambda_1\bar{z}\frac{J_0(\lambda_1\bar{r})}{\beta J_1(\lambda_1\beta)}\boldsymbol{e}_z$$
$$= -\kappa\frac{J_1(\lambda_1\bar{r})}{\beta J_1(\lambda_1\beta)}\boldsymbol{e}_r + \lambda_1\kappa\bar{z}\frac{J_1(\lambda_1\bar{r})}{\beta J_1(\lambda_1\beta)}\boldsymbol{e}_\theta + \lambda_1\kappa\bar{z}\frac{J_0(\lambda_1\bar{r})}{\beta J_1(\lambda_1\beta)}\boldsymbol{e}_z \tag{2.17}$$

and

$$\bar{\psi} = \kappa\bar{z}\,\bar{r}\frac{J_1(\lambda_1\bar{r})}{\beta J_1(\lambda_1\beta)}, \tag{2.18}$$

where $\kappa \equiv (2\pi\sigma l)^{-1} = A_i/(2\pi a L) = 0.35355a/(SL)$, and $S = (\pi/\sqrt{2})\sigma \approx 2.22\sigma$ refers to the classical swirl number. Equation (2.17) encapsulates one type of behaviour that may be associated with the stream function. Accordingly, all three components of the velocity appear at the same order. While we continue to study the behaviour of (2.17), we are inclined to search for other possible forms that can unfold under different inlet and wall boundary conditions. Additionally, the axial variation of the stream function will warrant special examination in view of the trigonometric solutions in (2.8).

3. Fundamental characteristics

3.1. Theoretical locations of the mantle

The cylindrical mantle or spinning wheel refers to the axially rotating layer that separates the updraft (or inner vortex) from the downdraft (or outer vortex). It represents one of the key characteristic features of cyclones. Along this surface, one may set $u_z = 0$ and solve for the corresponding radial position $\bar{r} = \beta^*$. One readily obtains $J_0(\lambda_1\beta^*) = 0$ or $\beta^* = 0.627\,612$. This result differs from the 0.707 value obtained previously by Vyas and Majdalani (2006). In fact, it concurs with one of the two mantle locations reported by Smith (1962a, 1962b) and other numerical simulations carried out using a right-cylindrical chamber. It also stands more or less in line with the average value of $\beta^* \approx 0.675$ predicted by Hoekstra *et al* (1999). Note that these researchers' experimental and numerical tests were carried out at a moderate Reynolds number of $Re = 5 \times 10^4$ and three decreasing swirl numbers of $S = 3.1$, 2.2 and 1.8. The small deviations from our predicted value may be attributed to their specific use of a Reynolds stress transport model and to inevitable differences that are mainly germane to industrial prototypes of gas cyclones. In comparison to other investigations of cylindrical cyclones, the most notable may be the classical experiments by Smith (1962a, 1962b) who studied, with the aid of smoke, the formation of laminar vortex structures in a right-cylindrical cyclone comprising a flat bottom and a vortex finder. Based on the two main test cases reported in Smith's work, the experimental mantle measurements are catalogued in table 1 at several axial positions. It is gratifying that not only do his values exhibit weak sensitivity to the distance from the headwall, they also corroborate the duality of roots obtained so far, especially that his averages fall at approximately 0.62 and 0.72. These measurements compare quite favourably with the 0.63 and 0.71 mantle locations predicted by the presently derived and complex lamellar models, respectively. Concerning the weak sensitivity of mantle excursions to inlet flow conditions, confirmatory studies have been independently reported by Vatistas *et al* (1986a, 1986b), and by in-house studies including those by Fang *et al* (2003, 2004). As for the inception of multidirectional flow passes, the physical set of higher order

Table 1. Experimental mantle location according to Smith (1962a, 1962b).

Site no.	Position $L-z$ (inch)	Case I ($2''$ inlet) r (inch)	β^*	Case II ($0.5''$ inlet) r (inch)	β^*
1	0.0	1.99	0.6633	2.13	0.7083
2	1.5	1.89	0.6300	2.15	0.7166
3	3.0	1.88	0.6266	2.15	0.7166
4	4.5	1.85	0.6166	2.15	0.7166
5	6.0	1.79	0.5966	2.17	0.7233
6	7.5	1.79	0.5966	2.20	0.7333
7	9.0	1.75	0.5833	2.20	0.7333
Mean		1.85	0.6166	2.16	0.7211

Table 2. Matrix of mantle locations associated with the Beltramian and Trkalian motions.

m	$n=1$	$n=2$	$n=3$	$n=4$	$n=5$
1	$\beta_{1,1}=0.6276$				
2	$\beta_{2,1}=0.342\,783$	$\beta_{2,2}=0.786\,831$			
3	$\beta_{3,1}=0.236\,382$	$\beta_{3,2}=0.542\,596$	$\beta_{3,3}=0.850\,617$		
4	$\beta_{4,1}=0.180\,492$	$\beta_{4,2}=0.414\,305$	$\beta_{4,3}=0.649\,499$	$\beta_{4,4}=0.885\,005$	
5	$\beta_{5,1}=0.146\,007$	$\beta_{5,2}=0.335\,147$	$\beta_{5,3}=0.525\,404$	$\beta_{5,4}=0.715\,913$	$\beta_{5,5}=0.906\,518$

mantle locations may be extracted directly from (2.10). For the reader's convenience, these are summarized in table 2.

3.2. Characteristic properties

To avoid corner collisions in the exit plane, the chamber opening may be taken such that the open fraction is set to coincide with the mantle location, $\beta=\beta^*=0.627\,612$. By aligning the outflow diameter with the opening at $\bar{z}=l$, undesirable flow circulation and secondary flow formation are mitigated. The optimal solution simplifies into

$$\begin{aligned}\bar{\psi}&=c\kappa\bar{z}\,\bar{r}\,J_1(\lambda_1\bar{r})=3.069\kappa\bar{z}\,\bar{r}\,J_1(\lambda_1\bar{r}),\\ \bar{\boldsymbol{u}}&=-c\kappa J_1(\lambda_1\bar{r})\,\boldsymbol{e}_r+c\lambda_1\kappa\bar{z}J_1(\lambda_1\bar{r})\,\boldsymbol{e}_\theta+c\lambda_1\kappa\bar{z}J_0(\lambda_1\bar{r})\,\boldsymbol{e}_z\\ &=-3.069\kappa J_1(\lambda_1\bar{r})\,\boldsymbol{e}_r+11.76\kappa\bar{z}J_1(\lambda_1\bar{r})\,\boldsymbol{e}_\theta+11.76\kappa\bar{z}J_0(\lambda_1\bar{r})\,\boldsymbol{e}_z,\end{aligned}\tag{3.1}$$

where $c\equiv 1/[\beta J_1(\lambda_1\beta)]$ in general, and $c=3.069148$ for the particular case of $\beta=\beta^*$. From this expression, the radial crossflow velocity along the mantle may be calculated to be

$$(\bar{u}_r)_{\text{cross}}=-1.59334\kappa,\tag{3.2}$$

which is 12.7% larger (in magnitude) than the previously estimated value of $(\bar{u}_r)_{\text{cross}}=-1.41421\kappa, \forall z$ (cf Vyas and Majdalani 2006). Furthermore, a simple check of $2\pi\beta l\,|(\bar{u}_r)_{\text{cross}}|=\bar{Q}_i$ confirms that the entire mass entering the chamber is transported from the annular region into the inner vortex, uniformly along the mantle, before exiting at $\bar{z}=l$. Interestingly, both tangential and radial velocities reach their peak magnitudes at the same value of $\bar{r}_{\min}$ where

$$J_0(\lambda_1\bar{r}_{\min})-J_2(\lambda_1\bar{r}_{\min})=0.\tag{3.3}$$

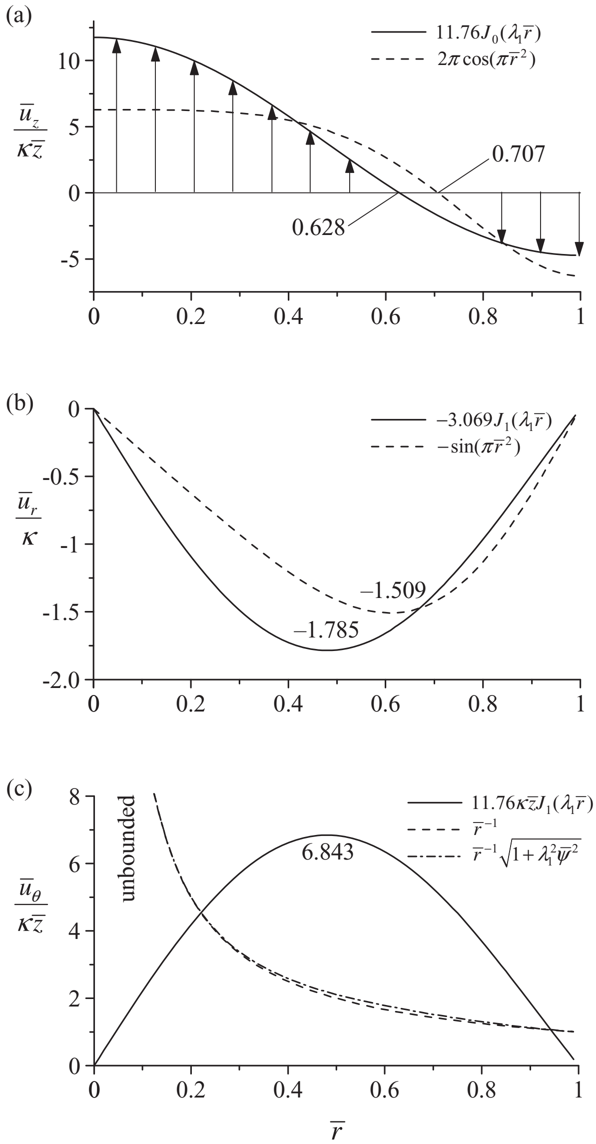

Figure 2. Examples of (a) axial, (b) radial, and (c) tangential velocity distributions.

Thus for $\bar{r}_{\min} = 0.480513$ we find $(\bar{u}_r)_{\min} = -1.78583\kappa$ to be comparable in size to the complex lamellar value of -1.50879κ. As for the tangential velocity, its maximum is no longer infinite but rather prescribed by the location and inflow parameter: $(\bar{u}_\theta)_{\max} = 6.84278\kappa\bar{z}$. This result is interesting as it suggests that $\bar{u}_\theta$, in its purely inviscid form, may be non-singular along the axis of rotation.

In the interest of clarity, normalized forms of the axial, radial, and tangential velocities are presented in figure 2 where they are also compared to the trigonometric profile

$$\bar{\boldsymbol{u}} = -\kappa\bar{r}^{-1}\sin(\pi\bar{r}^2)\boldsymbol{e}_r + \bar{r}^{-1}\boldsymbol{e}_\theta + 2\pi\kappa\bar{z}\cos(\pi\bar{r}^2)\boldsymbol{e}_z. \tag{3.4}$$

In hindsight, this trigonometric solution may be viewed as a pseudo-member of the family of complex lamellar flows, which are judiciously described by Truesdell (1954). This particular designation may be justified by virtue of the small helicity density, $\bar{\boldsymbol{\omega}} \cdot \bar{\boldsymbol{u}} = 4\pi^2 \kappa \bar{z} \sin(\pi \bar{r}^2)$, which causes streamlines to evolve nearly perpendicularly to vorticity lines, especially as κ becomes small (i.e., with high swirl), and whenever $\bar{r} = (0, 1)$. Moreover, the axial and radial components remain decoupled from the tangential motion, thus forming a strictly complex lamellar vector field, which is characterized by $\bar{\boldsymbol{\omega}} \cdot \bar{\boldsymbol{u}} = 0$. In the present case, axial rotation is simply imposed on the axisymmetric $(\bar{r}, \bar{z})$ motion. Finally, the derivation of (3.4) mirrors the approach used to extract the complex lamellar, Taylor–Culick profile, which is obtainable directly from Euler's equation (Majdalani and Saad 2007). Along similar lines, (3.4) may be straightforwardly retrieved from (2.1) by setting $B = aU$ and $\mathrm{d}H/\mathrm{d}\psi = -C^2\psi$. As before, the axial velocity shown in figure 2(a) varies linearly with $\bar{z}$, from a vanishingly small value at the headwall, to a maximum that occurs at the centre of the exit plane. In relative comparison to the complex lamellar solution, the centreline velocity amplification ascribed to the present model may be readily deduced from $11.76 J_0(0) / [2\pi \cos(0)] = 1.872$.

Surely, the 87.2% amplification in the maximum axial velocity may be confirmed graphically. As for the radial velocity magnitude, it vanishes at the sidewall and increases inwardly, thus peaking shortly after crossing the mantle, halfway along the radius ($\bar{r}_{\min} = 0.480\,513$). Subsequently, $|\bar{u}_r|$ decreases until fully disappearing along $\bar{r} = 0$ (see figure 2(b)).

The comparison for the self-similar swirl velocity is showcased in figure 2(c) side-by-side with the free vortex expression. While the latter remains insensitive to $\kappa\bar{z}$, the present model varies with the axial position and the tangential inflow parameter, thus peaking in the exit plane. It also comprises two evenly balanced regions that are somewhat reminiscent of the forced and free vortex regions, except for the relative size of the forced vortex, which is traditionally the smaller of the two. In relation to numerically simulated data available in the literature, $(\bar{u}_\theta)_{\max}$ seems to overpredict the maximum swirl detected at four axial positions. This behaviour may be attributed to the present model being purely inviscid and to viscous stresses constituting an important damping agent that cannot be captured here.

Having briefly sketched the principal velocities, the pressure gradients that accompany them may be extracted from Euler's equations viz.

$$\begin{aligned}\frac{\partial \bar{p}}{\partial \bar{r}} &= c^2\kappa^2 \left[\frac{(1+\lambda_1^2\bar{z}^2)}{\bar{r}} J_1^2(\lambda_1\bar{r}) - \lambda_1 J_1(\lambda_1\bar{r}) J_0(\lambda_1\bar{r}) \right] \\ &\approx -\frac{1}{4}c^2\lambda_1^2\kappa^2\bar{r}\left[1 - \frac{1}{2}\lambda_1^2\bar{r}^2 + \frac{5}{64}\lambda_1^4\bar{r}^4 - \lambda_1^2\bar{z}^2\left(1 - \frac{1}{4}\lambda_1^2\bar{r}^2 + \frac{5}{192}\lambda_1^4\bar{r}^4\right)\right],\end{aligned} \tag{3.5}$$

$$\frac{\partial \bar{p}}{\partial \bar{z}} = -c^2\lambda_1^2\kappa^2\bar{z}[J_0^2(\lambda_1\bar{r}) + J_1^2(\lambda_1\bar{r})] \approx -c^2\lambda_1^2\kappa^2\bar{z}\left(1 - \frac{1}{4}\lambda_1^2\bar{r}^2 + \frac{1}{32}\lambda_1^4\bar{r}^4 - \frac{5}{2304}\lambda_1^6\bar{r}^6\right) + \cdots. \tag{3.6}$$

Thus using $\bar{p}_0$ for the normalized pressure at $\bar{z} = 0$ and $\bar{r} = 1$, we can write $\Delta\bar{p} = \bar{p} - \bar{p}_0$ and integrate (3.5) and (3.6). This operation yields

$$\begin{aligned}\Delta\bar{p} &= -\frac{1}{2}c^2\kappa^2\{J_1^2(\lambda_1\bar{r}) + \lambda_1^2\bar{z}^2[J_0^2(\lambda_1\bar{r}) + J_1^2(\lambda_1\bar{r})]\} \\ &\approx -\frac{1}{8}c^2\lambda_1^2\kappa^2\left[\bar{r}^2 - \frac{1}{4}\lambda_1^2\bar{r}^4 + \frac{5}{192}\lambda_1^4\bar{r}^6 + \bar{z}^2\left(4 - \lambda_1^2\bar{r}^2 + \frac{1}{8}\lambda_1^4\bar{r}^4 - \frac{5}{576}\lambda_1^6\bar{r}^6\right) + \cdots\right].\end{aligned} \tag{3.7}$$

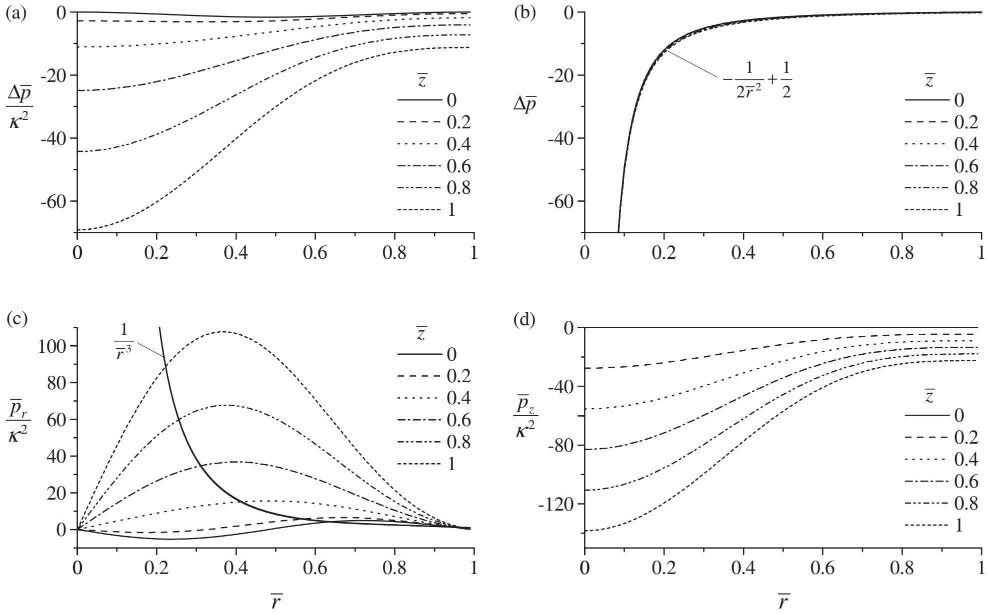

Figure 3. Pressure differential for (a) slip resistant Trkalian and (b) slip permitting Beltramian cases using $\upsilon = 0$. Corresponding radial and axial pressure gradients are shown in (c), (d) at several axial positions. Both solutions share the same axial pressure gradient.

Figure 3(a) illustrates the radial variation of $\Delta\bar{p}/\kappa^2$ at several axial stations that are evenly distributed along the chamber length. Being referenced to its value at $\bar{z} = 0$, the pressure differential varies from a small value at the headwall to $-69.2\kappa^2$ at $\bar{z} = 1$. Its prediction differs markedly from the $-\frac{1}{2}\bar{r}^{-2}$ behaviour shown in figure 3(b) (and associated with free vortex motion). The pressure gradients in the radial and axial directions are further shown in figures 3(c) and (d). Note that the locus of the peak radial pressure gradient is centralized, ranging between $\bar{r} = 0.722\,183$ and $0.355\,474$ for $0 \leqslant \bar{z} \leqslant 2.922\,24$. Despite the apparently large pressure gradients, actual magnitudes are reasonably tempered owing to the impending multiplication by κ^2. As we move downstream, the axial pressure gradient changes rapidly along the centreline and gradually along the sidewall. This behaviour may be viewed as an improvement over the $\partial\bar{p}/\partial\bar{z} = -4\pi^2\kappa^2\bar{z}$ relation associated with the complex lamellar model. The latter remains radially invariant while changing linearly with the distance from the headwall. The elevated pressure gradient in the central region suggests a faster moving core flow which, in turn, could be a performance enhancer.

To capture the two related solutions side-by-side, their streamlines are plotted in figure 4 using two chamber aspect ratios. It is interesting to note the strong similarities between the two motions despite the slight shift in their flow turning points. In fact, the two families of streamlines shown in the $\bar{r} - \bar{z}$ plane seem to mirror each other almost identically. The superimposition of swirl causes fluid particles entering the chamber to spin around while scooping down the chamber bore. Their motion is accompanied by uniform mass transport along the (chained) interface that separates the annular downdraft from the tubular updraft. Although not shown, the swirling speed of the returning stream increases with the distance from the headwall because of the angular momentum that it carries inwardly and the merging with the radial mass crossing the mantle. This behaviour is corroborated by several reported

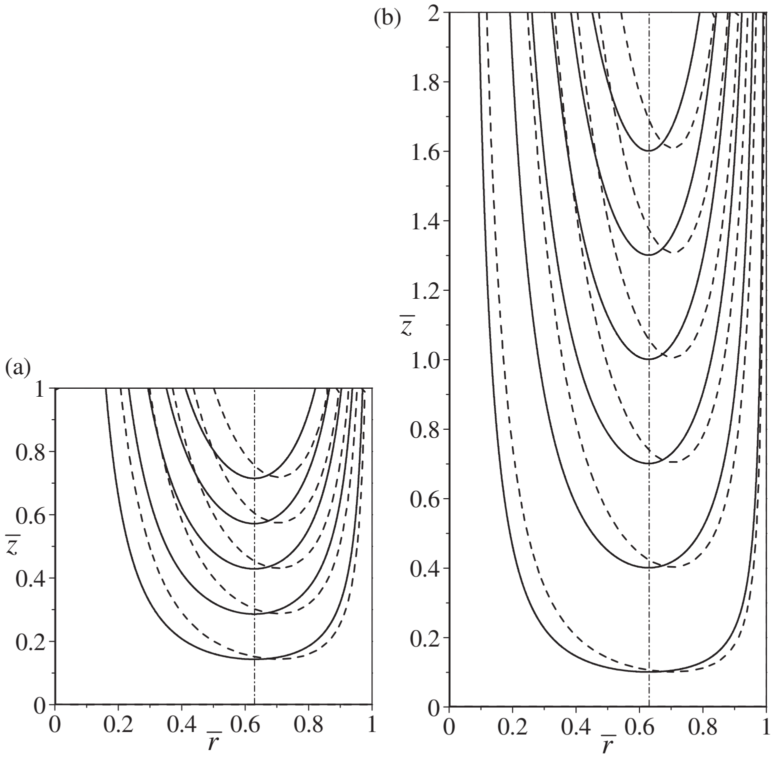

Figure 4. Flow streamlines comparing the present model (solid lines) to the complex lamellar solution (broken lines). Results are shown for two chamber aspect ratios of (a) $l = 1$ and (b) $l = 2$.

experiments and numerical simulations including those by Smith (1962a, 1962b), Hoekstra *et al* (1999), Anderson *et al* (2003) and Hu *et al* (2005). The vorticity and swirling intensity convected along with the flow can also be examined. The latter may be evaluated directly according to Chang and Dhir (1995) by taking

$$\tilde{\Omega} = \frac{1}{4}\int_0^{\beta} \bar{u}_z \bar{u}_\theta \bar{r}\,\mathrm{d}\bar{r}\left(\int_0^{\beta} \bar{u}_z \bar{r}\,\mathrm{d}\bar{r}\right)^{-2}$$
$$= \frac{1}{24}\beta\lambda_1^3 {}_2F_3\left[\left(\frac{3}{2},\frac{3}{2}\right),\left(2,2,\frac{5}{2}\right),-\beta^2\lambda_1^2\right] J_1^{-2}(\beta\lambda_1) \approx 1.340\,67. \qquad (3.8)$$

The constancy of the swirling intensity stands in sharp contrast to the spatially varying value of $5.443\sigma l/\bar{z}$, which accompanies the complex lamellar solution. Instead of peaking near the headwall or increasing with the swirl number as before, the present formulation yields a uniformly distributed swirling intensity throughout the chamber volume, irrespective of inlet conditions. This situation can be interpreted as a condition that is conducive of spatial constancy in mixing intensity. Graphically, the pitch angle of a spiralling streamline will be more uniform than its complex lamellar counterpart, which is known to vary from a small angle at the headwall to a large value over the body of the cylinder.

Another distinguishing attribute may be examined by evaluating the vorticity. This may be readily achieved using $\bar{\boldsymbol{\omega}} = \nabla \times \bar{\boldsymbol{u}}$ or

$$\begin{aligned}\bar{\boldsymbol{\omega}} &= -c\lambda_1\kappa J_1(\lambda_1\bar{r})\,\boldsymbol{e}_r + c\lambda_1^2\kappa\bar{z}J_1(\lambda_1\bar{r})\,\boldsymbol{e}_\theta + c\lambda_1^2\kappa\bar{z}J_0(\lambda_1\bar{r})\,\boldsymbol{e}_z \\ &= -11.7601\kappa J_1(\lambda_1\bar{r})\,\boldsymbol{e}_r + 45.0611\bar{z}J_1(\lambda_1\bar{r})\,\boldsymbol{e}_\theta + 45.0611\bar{z}J_0(\lambda_1\bar{r})\,\boldsymbol{e}_z.\end{aligned} \quad (3.9)$$

In the same vein, the vorticity magnitude may be estimated from

$$\bar{\omega} = c\lambda_1\kappa J_1(\lambda_1\bar{r})\sqrt{1+\lambda_1^2\bar{z}^2\left[1+J_0^2(\lambda_1\bar{r})/J_1^2(\lambda_1\bar{r})\right]}. \quad (3.10)$$

This result is substantially different from the swirl dominated complex lamellar solution which, in retrospect, was somewhat limited in that it could only engender one component of vorticity, namely, $\bar{\omega}_\theta = 4\pi^2\kappa\bar{r}\bar{z}\sin(\pi\bar{r}^2)$. The two additional components of vorticity that emerge here stem from the axial dependence of $\bar{u}_\theta$. At first glance, it may be inferred that (3.9) bears a striking resemblance to (3.1). Upon further scrutiny, however, we find the vorticity to be directly proportional to the velocity through $\bar{\boldsymbol{\omega}} = \lambda_1\bar{\boldsymbol{u}}$. This vector parallelism is accompanied by a vanishing Lamb vector ($\bar{\boldsymbol{\omega}} \times \bar{\boldsymbol{u}} = 0$), a defining characteristic of the Beltramian family of fluid motions in which the main source of nonlinearity is eliminated. The corresponding Helmholtz equation is linearized, thus giving rise to simple exact solutions of swirling motions (see Wu *et al* 2006). Note that the velocity in $\nabla \times \bar{\boldsymbol{u}} = \lambda_1\bar{\boldsymbol{u}}$ plays the role of an eigenvector of the curl operator connected with the eigenvalue λ_1. Within this class of helical fields, our flow may be specifically termed Trkalian because of the constancy of λ_1 (Aris 1962). Being a Trkalian profile, it forms a basis vector for helical wave decomposition that may be suitably adopted to represent steady, incompressible, and chaotic motions in a frictionless environment.

Figure 5(a) illustrates the vorticity distribution along the chamber cross section at select axial positions. Except for the region in the immediate vicinity of the headwall, it can be seen that vorticity is amplified near the centreline and continues to grow in the downstream direction. This behaviour is corroborated in figure 5(b) where contours of isovorticity are presented in the $\bar{r}-\bar{z}$ plane. In relative proportion to the azimuthal vorticity of its complex lamellar predecessor, the most significant differences arise in the core region and the immediate vicinity of the wall.

3.3. Solution for a non-vanishing circumferential velocity

In the foregoing analysis, the swirl velocity was made to artificially vanish at the sidewall. However, such a condition is expendable in a frictionless environment. In mirroring the complex lamellar solution, one may take $u_\theta(a, L) = U$ such that $B_1 = U^2a^2$ may be retrieved from (2.4). This condition only affects the tangential component of the velocity by changing it into

$$u_\theta = \frac{1}{r}\left[\psi_0^2\lambda_1^2r^2\left(\frac{z}{a}\right)^2 J_1^2\left(\lambda_1\frac{r}{a}\right) + U^2a^2\right]^{1/2}, \quad (3.11)$$

where (3.11) refers to a solution that permits slip at the sidewall and, for similar reasons, becomes unbounded at the centreline. Suppressing the inherent singularity at $r = 0$ will have to be achieved using a suitable boundary layer treatment. Note that u_θ is strongly dominated by the free vortex behaviour of its leading order part and displays only weak dependence on

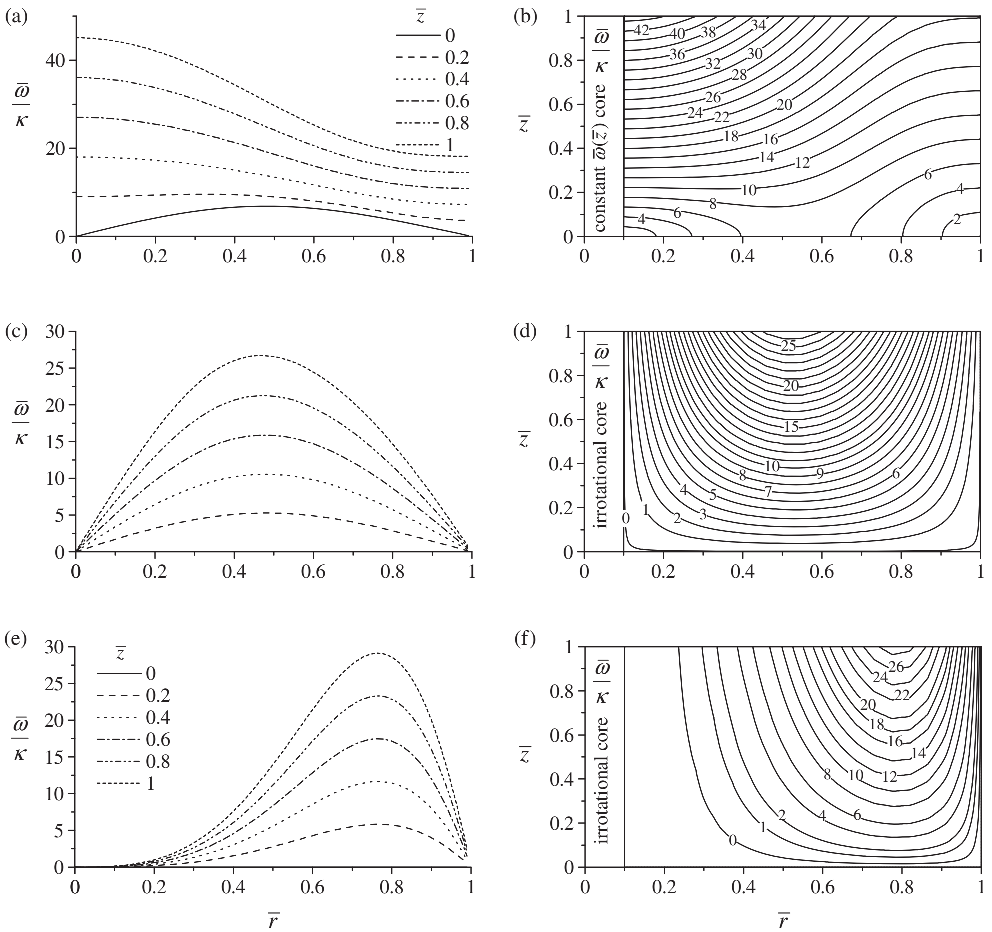

Figure 5. Radial distribution of total vorticity along (a) fixed axial positions and (b) isolines. The same is repeated in (c), (d) for the slip permitting Beltramian solution, and in (e), (f) for the complex lamellar model.

the spatially varying stream function. In dimensionless form, (3.11) collapses into

$$\bar{u}_\theta = \frac{\bar{B}}{\bar{r}} = \frac{1}{\bar{r}}\sqrt{1+\lambda_1^2\bar{\psi}^2} = \frac{1}{\bar{r}}\left[1+\frac{\lambda_1^2\kappa^2\bar{r}^2\bar{z}^2 J_1^2(\lambda_1\bar{r})}{\beta^2 J_1^2(\lambda_1\beta)}\right]^{1/2} = \frac{1}{\bar{r}}\sqrt{1+c^2\lambda_1^2\kappa^2\bar{r}^2\bar{z}^2 J_1^2(\lambda_1\bar{r})}. \tag{3.12}$$

Before evaluating the induced pressure and vorticity, it may be useful to express the complete solution via

$$\bar{\boldsymbol{u}} = -3.069\kappa J_1(\lambda_1\bar{r})\,\boldsymbol{e}_r + \frac{1}{\bar{r}}\left[1+138.3\kappa^2\bar{r}^2\bar{z}^2 J_1^2(\lambda_1\bar{r})\right]^{1/2}\boldsymbol{e}_\theta + 11.76\kappa\bar{z}J_0(\lambda_1\bar{r})\,\boldsymbol{e}_z. \tag{3.13}$$

We mention in passing that the axisymmetric streamlines associated with (3.13) coincide with the solid curves shown in the $\bar{r}-\bar{z}$ plane of figure 4. As for the corresponding radial and axial pressure gradients, these may be readily extracted from Euler's momentum equation.

We find, in relation to the just computed solution with no slip,

$$\frac{\partial \bar{p}}{\partial \bar{r}} = \left(\frac{\partial \bar{p}}{\partial \bar{r}}\right)_{\rm noslip} + \bar{r}^{-3} = \frac{1 + c^2\kappa^2\bar{r}^2 J_1(\lambda_1\bar{r})\left[(1+\lambda_1^2\bar{z}^2)J_1(\lambda_1\bar{r}) - \lambda_1\bar{r}J_0(\lambda_1\bar{r})\right]}{\bar{r}^3}$$

$$\approx \bar{r}^{-3} - \frac{1}{4}c^2\lambda_1^2\kappa^2\bar{r}\left[1 - \frac{1}{2}\lambda_1^2\bar{r}^2 + \frac{5}{64}\lambda_1^4\bar{r}^4 - \frac{7}{1152}\lambda_1^6\bar{r}^6 - \lambda_1^2\bar{z}^2 \times\left(1 - \frac{1}{4}\lambda_1^2\bar{r}^2 + \frac{5}{192}\lambda_1^4\bar{r}^4 - \frac{7}{4608}\lambda_1^6\bar{r}^6\right)\right], \tag{3.14}$$

$$\frac{\partial \bar{p}}{\partial \bar{z}} = \left(\frac{\partial \bar{p}}{\partial \bar{z}}\right)_{\rm noslip} = -c^2\lambda_1^2\kappa^2\bar{z}[J_0^2(\lambda_1\bar{r}) + J_1^2(\lambda_1\bar{r})]$$

$$\approx -c^2\kappa^2\lambda_1^2\bar{z}\left(1 - \frac{1}{4}\lambda_1^2\bar{r}^2 + \frac{1}{32}\lambda_1^4\bar{r}^4 - \frac{5}{2304}\lambda_1^6\bar{r}^6\right) + \cdots. \tag{3.15}$$

Then using $\bar{p}_0$ for the normalized pressure at $(1, 0)$, partial integration towards $\Delta\bar{p} = \bar{p} - \bar{p}_0$ leads to

$$\Delta\bar{p} = (\Delta\bar{p})_{\rm noslip} - \frac{1}{2}\bar{r}^{-2} = -\frac{1}{2}\bar{r}^{-2} - \frac{1}{2}c^2\kappa^2\{J_1^2(\lambda_1\bar{r}) + \lambda_1^2\bar{z}^2[J_0^2(\lambda_1\bar{r}) + J_1^2(\lambda_1\bar{r})]\} + \frac{1}{2}$$

$$\approx -\frac{1}{2}\bar{r}^{-2} - \frac{1}{8}c^2\lambda_1^2\kappa^2\left[\bar{r}^2 - \frac{1}{4}\lambda_1^2\bar{r}^4 + \frac{5}{192}\lambda_1^4\bar{r}^6 + \bar{z}^2 \times\left(4 - \lambda_1^2\bar{r}^2 + \frac{1}{8}\lambda_1^4\bar{r}^4 - \frac{5}{576}\lambda_1^6\bar{r}^6\right) + \cdots\right] + \frac{1}{2}. \tag{3.16}$$

Unlike figure 3(a) in which the pressure variation remains finite, $\Delta\bar{p}$ is largely dominated by the sharp sloping $-\frac{1}{2}\bar{r}^{-2}$ distribution depicted in figure 3(b). Furthermore, owing to the free vortex divergence near the axis of rotation, the radial pressure gradient is seen to be controlled by the inverse $\bar{r}^{-3}$ power law captured in figure 3(c). This behaviour is identical to that associated with the complex lamellar solution. As for the axial pressure gradient, it remains independent of the swirl velocity and is suitably described in figure 3(d).

Lastly for this case, the mean flow vorticity may be directly evaluated and simplified into

$$\bar{\boldsymbol{\omega}} = -\frac{138.3\kappa^2\bar{r}\bar{z}J_1^2(\lambda_1\bar{r})}{\sqrt{1 + 138.3\kappa^2\bar{r}^2\bar{z}^2J_1^2(\lambda_1\bar{r})}}\boldsymbol{e}_r + 45.06\kappa\bar{z}J_1(\lambda_1\bar{r})\,\boldsymbol{e}_\theta + \frac{529.92\kappa^2\bar{r}\bar{z}^2J_0(\lambda_1\bar{r})\,J_1(\lambda_1\bar{r})}{\sqrt{1 + 138.3\kappa^2\bar{r}^2\bar{z}^2J_1^2(\lambda_1\bar{r})}}\boldsymbol{e}_z. \tag{3.17}$$

As expected, we find the spatial distribution of vorticity to be dominated by its tangential component $\bar{\omega}_\theta$. This, in turn, mirrors the tangential velocity given by (3.1), except for its magnitude being 3.832 times larger. Forthwith, the radial distribution of $\bar{\omega}/\kappa$ is illustrated in figure 5(c) at several axial stations. It is clear that the vorticity vanishes at the headwall, sidewall, and centreline, where an irrotational vortex is established. The onset of an irrotational core about the z-axis is further corroborated by the contour plots of isovorticity rendered in figure 5(d). These confirm that vorticity increases in the positive downstream direction and reaches its peak value at $\bar{r}_{max} = 0.480\,513$. In fact, the maximum vorticity at any axial station may be readily calculated from

$$\bar{\omega}_{max} = 26.22\kappa\bar{z}\left[1 + 2.1749\kappa^2(0.338\,567 + 6.437\,17\bar{z}^2)\right]^{\frac{1}{2}} / \left(1 + 10.811\kappa^2\bar{z}^2\right)^{\frac{1}{2}} \geqslant 26.22\kappa\bar{z}. \tag{3.18}$$

It is perhaps instructive to note that the vorticity distribution associated with (3.17) is spread over a relatively wide chamber interval despite its inclusion of an irrotational core. This is especially true when compared to the vorticity generated by the complex lamellar profile. The latter is described in figures 5(e) and (f) where a major vorticity concentration is located away from the centreline, thus leading to a substantially wider irrotational core region. By comparing the various contours in figure 5, it appears that the solutions discussed above exhibit from top to bottom, increasingly wider irrotational segments. While (3.11) corresponds to a Beltramian flow with $\bar{\boldsymbol{\omega}} \times \bar{\boldsymbol{u}} = 0$, it remains non-Trkalian because of its spatially varying ratio of vorticity and velocity, namely,

$$\frac{\bar{\boldsymbol{\omega}}}{\bar{\boldsymbol{u}}} = \lambda_1\left[1 + \frac{1}{c^2\kappa^2\lambda_1^2\bar{r}^2\bar{z}^2 J_1^2(\lambda_1\bar{r})}\right]^{-1/2}. \tag{3.19}$$

For the reader's convenience, the principal equations associated with the $\upsilon = 0$ case are catalogued in table 3 for both Beltramian and Trkalian fields.

4. Other similarity conforming solutions

Pursuant to (2.8), two practically equivalent forms of solution may be worthwhile to investigate. These are

$$\psi(r,z) = \begin{cases} \psi_0\, r\sin(\upsilon z) J_1(r\sqrt{C^2-\upsilon^2}), & \upsilon^2 \leqslant C^2, \\ \psi_0\, r\sinh(\upsilon z) J_1(r\sqrt{C^2+\upsilon^2}), & \upsilon^2 > C^2, \end{cases} \tag{4.1}$$

where we have set $c_2 = 0$ and $c_4 = 0$ to satisfy $u_z(r,0) = 0$ and $u_r(0,z) = 0$ in (2.9), respectively. We have also taken $\psi_0 \equiv c_1 c_3$ with no loss of generality. The third condition left to be applied consists of $u_r(a,z) = 0$. Hence, we have

$$\frac{\partial\psi(a,z)}{\partial z} = \begin{cases} \psi_0\, a\upsilon\cos(\upsilon z) J_1(a\sqrt{C^2-\upsilon^2}) = 0, & \upsilon^2 \leqslant C^2, \\ \psi_0\, a\upsilon\cosh(\upsilon z) J_1(a\sqrt{C^2+\upsilon^2}) = 0, & \upsilon^2 > C^2. \end{cases} \tag{4.2}$$

These constraints will be satisfied, $\forall z$, when

$$\begin{cases} J_1(a\sqrt{C^2-\upsilon^2}) = 0, \\ J_1(a\sqrt{C^2+\upsilon^2}) = 0, \end{cases} \quad \begin{cases} \sqrt{C^2-\upsilon^2} = \lambda_m/a, \\ \sqrt{C^2+\upsilon^2} = \lambda_m/a \end{cases} \quad \text{or} \quad \begin{cases} \upsilon^2 = C^2 - \lambda_m^2/a^2, \\ \upsilon^2 = \lambda_m^2/a^2 - C^2. \end{cases} \tag{4.3}$$

Here $m \in \mathbb{N}^*$ and $\lambda_m = \{3.831\,71, 7.015\,59, \ldots\}$ denote, as before, the roots of the Bessel function of the first kind. Due to the linearity of (2.6), a series solution can be realized by summing over all possible eigenmodes and a fixed value of C. Conversely, a partial solution may be obtained in closed form for a single flow reversal of a bidirectional vortex. By taking $\lambda_1 = 3.831\,71$, we deduce $C_1 = (\lambda_1^2/a^2 + \upsilon^2)^{1/2}$, where the separation constant υ may be determined from an additional physical constraint, such as $u_r(r,L) = 0$. This condition forces

Table 3. Beltramian and Trkalian cases with $\upsilon = 0$.

Variable	Equation
	Common parts
$\bar{\psi}$	$c\kappa\bar{z}\,\bar{r}\,J_1(\lambda_1\bar{r})$
$(\bar{u}_r)_{\text{cross}}$	-1.5933κ
$(\bar{u}_r)_{\min}$	-1.7858κ
$\dfrac{\partial\bar{p}}{\partial\bar{z}}$	$-c^2\lambda_1^2\kappa^2\bar{z}[J_0^2(\lambda_1\bar{r})+J_1^2(\lambda_1\bar{r})]$
	Trkalian case with no slip
$\bar{\boldsymbol{u}}$	$-c\kappa J_1(\lambda_1\bar{r})\,\boldsymbol{e}_r + c\lambda_1\kappa\bar{z}J_1(\lambda_1\bar{r})\,\boldsymbol{e}_\theta + c\lambda_1\kappa\bar{z}J_0(\lambda_1\bar{r})\,\boldsymbol{e}_z$
$\bar{\boldsymbol{\omega}}$	$-c\lambda_1\kappa J_1(\lambda_1\bar{r})\,\boldsymbol{e}_r + c\lambda_1^2\kappa\bar{z}J_1(\lambda_1\bar{r})\,\boldsymbol{e}_\theta + c\lambda_1^2\kappa\bar{z}J_0(\lambda_1\bar{r})\,\boldsymbol{e}_z$
$(\bar{u}_\theta)_{\max}$	$6.8428\kappa\bar{z}$
$\dfrac{\partial\bar{p}}{\partial\bar{r}}$	$c^2\kappa^2\left[\dfrac{(1+\lambda_1^2\bar{z}^2)}{\bar{r}}J_1^2(\lambda_1\bar{r})-\lambda_1 J_1(\lambda_1\bar{r})J_0(\lambda_1\bar{r})\right]$
$\Delta\bar{p}$	$-\dfrac{1}{2}c^2\kappa^2\{J_1^2(\lambda_1\bar{r})+\lambda_1^2\bar{z}^2[J_0^2(\lambda_1\bar{r})+J_1^2(\lambda_1\bar{r})]\}$
$\tilde{\Omega}$	$\frac{1}{24}\beta\lambda_1^3\,{}_2F_3\left[\left(\frac{3}{2},\frac{3}{2}\right),\left(2,2,\frac{5}{2}\right),-\beta^2\lambda_1^2\right]J_1^{-2}(\beta\lambda_1)\approx 1.340\,67$
	Beltramian case with slip
$\bar{\boldsymbol{u}}$	$-c\kappa J_1(\lambda_1\bar{r})\,\boldsymbol{e}_r + \frac{1}{\bar{r}}\sqrt{1+c^2\lambda_1^2\kappa^2\bar{r}^2\bar{z}^2J_1^2(\lambda_1\bar{r})}\,\boldsymbol{e}_\theta + c\lambda_1\kappa\bar{z}J_0(\lambda_1\bar{r})\,\boldsymbol{e}_z$
$\bar{\boldsymbol{\omega}}$	$-\dfrac{c^2\lambda_1^2\kappa^2\bar{r}\bar{z}J_1^2(\lambda_1\bar{r})}{\sqrt{1+c^2\lambda_1^2\kappa^2\bar{r}^2\bar{z}^2J_1^2(\lambda_1\bar{r})}}\boldsymbol{e}_r + c\lambda_1^2\kappa\bar{z}J_1(\lambda_1\bar{r})\,\boldsymbol{e}_\theta + \dfrac{c^2\lambda_1^3\kappa^2\bar{r}\bar{z}^2J_0(\lambda_1\bar{r})\,J_1(\lambda_1\bar{r})}{\sqrt{1+c^2\lambda_1^2\kappa^2\bar{r}^2\bar{z}^2J_1^2(\lambda_1\bar{r})}}\boldsymbol{e}_z$
$(\bar{u}_\theta)_{\max}$	∞
$\dfrac{\partial\bar{p}}{\partial\bar{r}}$	$\frac{1}{\bar{r}^3}+c^2\kappa^2\left[\dfrac{(1+\lambda_1^2\bar{z}^2)}{\bar{r}}J_1^2(\lambda_1\bar{r})-\lambda_1 J_1(\lambda_1\bar{r})J_0(\lambda_1\bar{r})\right]$
$\Delta\bar{p}$	$-\frac{1}{2}\bar{r}^{-2}-\frac{1}{2}c^2\kappa^2\{J_1^2(\lambda_1\bar{r})+\lambda_1^2\bar{z}^2[J_0^2(\lambda_1\bar{r})+J_1^2(\lambda_1\bar{r})]\}+\frac{1}{2}$

the radial velocity to vanish at the endwall where the modelled flow is purely tangential. At the outset, one collects, for the trigonometric profile,

$$\cos(\upsilon_j L)=0 \quad \text{or} \quad \upsilon_j=\left(j+\tfrac{1}{2}\right)\pi/L, \qquad j\in N. \tag{4.4}$$

To prevent the formation of undesirable recirculatory flows in the axial direction, we limit our attention to $\upsilon=\upsilon_0=\frac{1}{2}\pi/L$. We recognize that other forms exist but these may find applications in physical settings that fall outside the scope of this investigation. In what follows, we focus our attention on

$$\psi(r,z)=\psi_0 r\sin\left(\tfrac{1}{2}\pi z/L\right)J_1(\lambda_1 r/a), \quad C_1=\sqrt{\lambda_1^2/a^2+\tfrac{1}{4}\pi^2/L^2}. \tag{4.5}$$

The solution at this point may be expressed as

$$\boldsymbol{u} = -\frac{\pi\psi_0}{2L}\cos\left(\frac{\pi z}{2L}\right) J_1\left(\lambda_1\frac{r}{a}\right)\boldsymbol{e}_r + \frac{1}{r}\sqrt{\psi_0^2 r^2\left(\frac{\lambda_1^2}{a^2}+\frac{\pi^2}{4L^2}\right)\sin^2\left(\frac{\pi z}{2L}\right) J_1^2\left(\lambda_1\frac{r}{a}\right)+B_1}\,\boldsymbol{e}_\theta$$
$$+\frac{\psi_0}{a}\lambda_1\sin\left(\frac{\pi z}{2L}\right) J_0\left(\lambda_1\frac{r}{a}\right)\boldsymbol{e}_z, \tag{4.6}$$

where ψ_0 may be obtained from global mass conservation. We get

$$\psi_0 = Q_i\left[2\pi a\beta J_1(\lambda_1\beta)\right]^{-1}. \tag{4.7}$$

Concerning the last remaining constant, B_1, it will be either nil or U^2a^2, depending on whether we set $u_\theta(a,z)=0$, or U, respectively.

4.1. Axially nonlinear Trkalian solution with no slip

For the Trkalian motion that is compelled to satisfy no slip at $r=a$, the solution becomes

$$\begin{cases}
\psi = \dfrac{Q_i}{2\pi a\beta J_1(\lambda_1\beta)} r\sin\left(\dfrac{\pi z}{2L}\right) J_1\left(\lambda_1\dfrac{r}{a}\right), \\
u_r = -\dfrac{\pi Q_i}{4\pi a L\beta J_1(\lambda_1\beta)}\cos\left(\dfrac{\pi z}{2L}\right) J_1\left(\lambda_1\dfrac{r}{a}\right), \\
u_\theta = \dfrac{Q_i}{2\pi a\beta J_1(\lambda_1\beta)}\sqrt{\dfrac{\lambda_1^2}{a^2}+\dfrac{\pi^2}{4L^2}}\sin\left(\dfrac{\pi z}{2L}\right) J_1\left(\lambda_1\dfrac{r}{a}\right), \\
u_z = \dfrac{Q_i}{2\pi a^2\beta J_1(\lambda_1\beta)}\lambda_1\sin\left(\dfrac{\pi z}{2L}\right) J_0\left(\lambda_1\dfrac{r}{a}\right),
\end{cases}$$

and so,

$$\begin{cases}
\bar\psi = \dfrac{\kappa l}{\beta J_1(\lambda_1\beta)}\bar r\sin\left(\dfrac{\pi\bar z}{2l}\right) J_1(\lambda_1\bar r), \\
\bar u_r = -\dfrac{\pi}{2}\dfrac{\kappa}{\beta J_1(\lambda_1\beta)}\cos\left(\dfrac{\pi\bar z}{2l}\right) J_1(\lambda_1\bar r), \\
\bar u_\theta = \dfrac{\kappa}{\beta J_1(\lambda_1\beta)}\sqrt{\lambda_1^2 l^2+\dfrac{1}{4}\pi^2}\sin\left(\dfrac{\pi\bar z}{2l}\right) J_1(\lambda_1\bar r), \\
\bar u_z = \dfrac{\kappa l}{\beta J_1(\lambda_1\beta)}\lambda_1\sin\left(\dfrac{\pi\bar z}{2l}\right) J_0(\lambda_1\bar r).
\end{cases} \tag{4.8}$$

For the slip permitting Beltramian model, the profile will share the same components except for

$$u_\theta = \frac{1}{r}\sqrt{\left[\frac{Q_i}{2\pi a\beta J_1(\lambda_1\beta)}\right]^2 r^2\left(\frac{\lambda_1^2}{a^2}+\frac{\pi^2}{4L^2}\right)\sin^2\left(\frac{\pi z}{2L}\right) J_1^2\left(\lambda_1\frac{r}{a}\right)+U^2a^2} \tag{4.9}$$

or, in dimensionless form,

$$\bar u_\theta = \frac{1}{\bar r}\sqrt{\frac{\kappa^2}{\beta^2 J_1^2(\lambda_1\beta)}\left(\lambda_1^2 l^2+\frac{1}{4}\pi^2\right)\bar r^2\sin^2\left(\frac{\pi\bar z}{2l}\right) J_1^2(\lambda_1\bar r)+1}. \tag{4.10}$$

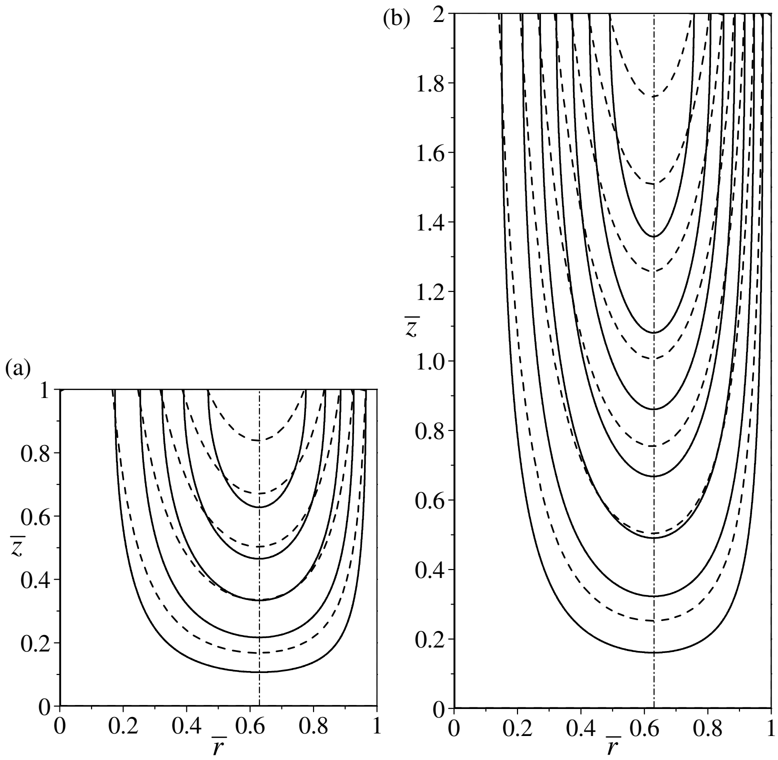

Figure 6. Streamlines for $\upsilon = \frac{1}{2}\pi/L$ (solid lines) and $\upsilon = 0$ (broken lines) using (a) $l = 1$ and (b) $l = 2$.

These two models share the same stream function shown in figure 6. In compact notation, we therefore have $\bar{\psi} = c\kappa l\,\bar{r}\sin\left(\frac{1}{2}\pi\bar{z}/l\right) J_1(\lambda_1\bar{r})$, and, starting with the velocity adhering Trkalian solution, we let $\bar{B} = (\lambda_1^2 + \frac{1}{4}\pi^2/l^2)^{1/2}\bar{\psi}$ so that

$$\bar{\boldsymbol{u}} = \begin{cases} -\frac{1}{2}\pi c\kappa\cos\left(\frac{1}{2}\pi\bar{z}/l\right) J_1(\lambda_1\bar{r})\,\boldsymbol{e}_r + \frac{1}{2}\pi c\kappa\sqrt{1+4\lambda_1^2 l^2/\pi^2}\sin\left(\frac{1}{2}\pi\bar{z}/l\right) J_1(\lambda_1\bar{r})\,\boldsymbol{e}_\theta \\ \quad + c\lambda_1\kappa l\sin\left(\frac{1}{2}\pi\bar{z}/l\right) J_0(\lambda_1\bar{r})\,\boldsymbol{e}_z \\ -4.821\kappa\cos\left(\frac{1}{2}\pi\bar{z}/l\right) J_1(\lambda_1\bar{r})\,\boldsymbol{e}_r + 4.821\sqrt{1+5.95l^2}\kappa\sin\left(\frac{1}{2}\pi\bar{z}/l\right) J_1(\lambda_1\bar{r})\,\boldsymbol{e}_\theta \\ \quad + 11.76\kappa l\sin\left(\frac{1}{2}\pi\bar{z}/l\right) J_0(\lambda_1\bar{r})\,\boldsymbol{e}_z. \end{cases} \tag{4.11}$$

The mantle here remains fixed at 0.6276. Moreover, by evaluating the axial velocity at the endwall, where $\bar{z} = l$, we recover $11.76\kappa l J_0(\lambda_1\bar{r})$. This local radial distribution is identical to that restored from (3.1) and displayed in figure 2(a). In contrast, the radial velocity vanishes at the endwall and peaks at the headwall with a value of $-4.821\kappa J_1(\lambda_1\bar{r})$. This outcome corresponds to 1.57 times its counterpart, $-3.069\kappa J_1(\lambda_1\bar{r})$, given by (3.1) (and shown in figure 2(b)). These medians given at $\bar{z} = \frac{1}{2}l$ reproduce $\bar{u}_z = 8.32\kappa l J_0(\lambda_1\bar{r})$ and $\bar{u}_r = -3.41\kappa J_1(\lambda_1\bar{r})$. These, in turn, exceed their counterparts in (3.1). We infer that both axial and radial velocities associated with this motion tend to exhibit larger magnitudes than those with $\upsilon = 0$, although they remain self-similar in the radial direction. This behaviour is further illustrated in figure 7 where the three velocity components are displayed.

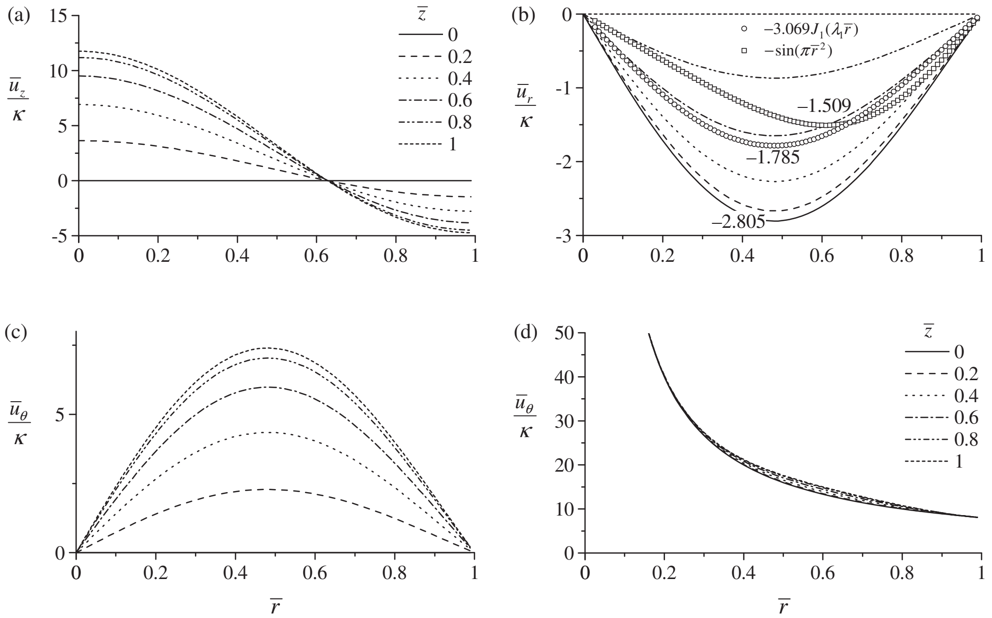

Figure 7. Examples of (a) axial, (b) radial and (c), (d) tangential velocity distributions based on (c) slip resistant Trkalian and (d) slip permitting Beltramian solutions. Here $\kappa = 0.125$ and $l = 1$ unless specified otherwise.

From (4.11), the radial crossflow velocity along the mantle may be calculated to be

$$(\bar{u}_r)_{\text{cross}} = -2.5028\kappa \cos\left(\tfrac{1}{2}\pi\bar{z}/l\right). \tag{4.12}$$

According to this model, the mass transfer across the mantle starts from zero at the endwall and increases in absolute value to a peak value of $[(\bar{u}_r)_{\text{cross}}]_{\min} = -2.5028\kappa$ at the headwall. In particular, given that $2(2.5028)\beta/\pi = 1$, one can verify that

$$2\pi\beta \int_0^l |(\bar{u}_r)_{\text{cross}}| \, \mathrm{d}\bar{z} = \sigma^{-1} = \bar{Q}_i. \tag{4.13}$$

In some propulsion-related applications, such as the class of vortex-fired engines, this particular variation is advantageous as it suggests a gradual increase in the inward spillage rate, namely, from the outer vortex into the inner vortex. If such a motion could be established in the VCCWC prototype, it would lead to a substantial reduction in early oxidizer leakage, a transport mechanism that ordinarily takes place immediately after injection. As for the peak radial velocity, it occurs at the same position defined by $\bar{r}_{\min} = 0.4805$. Its evaluation leads to

$$(\bar{u}_r)_{\min} = -2.8052\kappa \cos\left(\tfrac{1}{2}\pi\bar{z}/l\right). \tag{4.14}$$

Equation (4.14) also varies along the length of the chamber. The same may be said of the swirl velocity which peaks at $\bar{r}_{\max}$ with a value of

$$(\bar{u}_\theta)_{\max} = 2.8052\sqrt{1+5.9504l^2}\kappa \sin\left(\tfrac{1}{2}\pi\bar{z}/l\right) = 0.4465\sigma^{-1}\sqrt{l^{-2}+5.9504} \sin\left(\tfrac{1}{2}\pi\bar{z}/l\right). \tag{4.15}$$

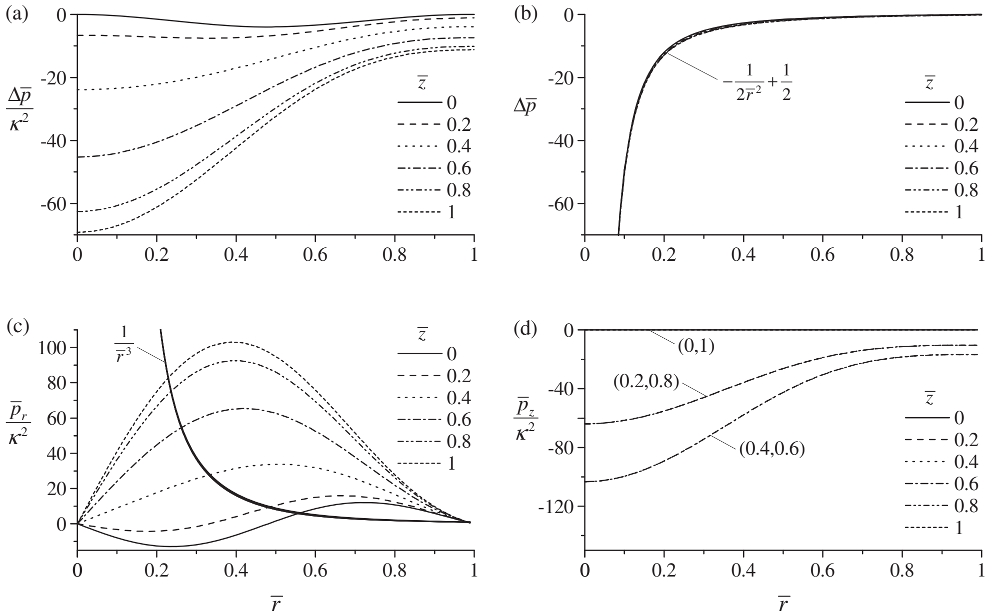

Figure 8. Pressure differential for (a) slip resistant Trkalian and (b) slip permitting Beltramian cases using $\upsilon = \frac{1}{2}\pi/L$. Corresponding radial and axial pressure gradients are shown in (c), (d) at several axial positions. Both solutions share the same axial pressure gradient. Here $\kappa = 0.125$ and $l = 1$ unless specified otherwise.

Through (4.15), it can be seen that $(\bar{u}_\theta)_{\max}$ will peak at entry and vanish at the headwall. While increasing the aspect ratio seems to have a secondary effect on the maximum swirl speed, the inverse relation between $(\bar{u}_\theta)_{\max}$ and the swirl number may be attributed to the boundary condition that artificially impedes the tangential velocity at the sidewall.

In mirroring the analysis of section 2, the pressure associated with this model can be determined from

$$\frac{\partial\bar{p}}{\partial\bar{r}} = \frac{1}{4}c^2\kappa^2 J_1(\lambda_1\bar{r})\left\{-\pi^2\lambda_1 J_0(\lambda_1\bar{r}) + \bar{r}^{-1}J_1(\lambda_1\bar{r})\left[\pi^2 + 2l^2\lambda_1^2 - 2l^2\lambda_1^2\cos(\pi\bar{z}/l)\right]\right\}, \tag{4.16}$$

$$\frac{\partial\bar{p}}{\partial\bar{z}} = -\frac{1}{4}\pi c^2\lambda_1^2\kappa^2 l[J_0^2(\lambda_1\bar{r}) + J_1^2(\lambda_1\bar{r})]\sin(\pi\bar{z}/l) \tag{4.17}$$

and so

$$\Delta\bar{p} = -\frac{1}{8}c^2\kappa^2\left\{\pi^2 J_1^2(\lambda_1\bar{r}) + 2\lambda_1^2 l^2[J_0^2(\lambda_1\bar{r}) + J_1^2(\lambda_1\bar{r})][1-\cos(\pi\bar{z}/l)]\right\}. \tag{4.18}$$

These expressions are evaluated and plotted in figure 8 where they appear to bear strong commonalities with the results of figure 3. Compared to the $\upsilon = 0$ solution, we find the pressure excursion and its gradients to be slightly higher, hence consistent with the accompanying increase in velocity magnitudes. The axial pressure gradient is particularly interesting due to its periodicity in $\bar{z}$. This is illustrated in figure 8(d) where the curves associated with the (0,1), (0.2,0.8), and (0.5,0.6) pairs of axial positions are seen to collapse into three individual lines that share identical values.

Next in line, the swirling intensity may be calculated for the $\upsilon \neq 0$ case. We get

$$\tilde{\Omega} = \frac{\beta\lambda_1^2\sqrt{\pi^2+4\lambda_1^2 l^2}\,{}_2F_3\left[\left(\frac{3}{2},\frac{3}{2}\right),\left(2,2,\frac{5}{2}\right),-\beta^2\lambda_1^2\right]}{48 l J_1^2(\beta\lambda_1)} \approx 0.549\,604\sqrt{1+5.9504 l^2}. \quad (4.19)$$

It is interesting that $\tilde{\Omega}$ grows in elongated chambers for which the length-to-diameter aspect ratio is increased. At this juncture, we turn our attention to the vorticity distribution and retrieve

$$\bar{\boldsymbol{\omega}} = -\tfrac{1}{2}c\pi\kappa\sqrt{\lambda_1^2+\tfrac{1}{4}\pi^2/l^2}\,J_1(\lambda_1\bar{r})\cos\left(\tfrac{1}{2}\pi\bar{z}/l\right)\boldsymbol{e}_r + c\kappa l(\lambda_1^2+\tfrac{1}{4}\pi^2/l^2)J_1(\lambda_1\bar{r})\sin\left(\tfrac{1}{2}\pi\bar{z}/l\right)\boldsymbol{e}_\theta$$
$$+c\kappa l\lambda_1\sqrt{\lambda_1^2+\tfrac{1}{4}\pi^2/l^2}\,J_0(\lambda_1\bar{r})\sin\left(\tfrac{1}{2}\pi\bar{z}/l\right)\boldsymbol{e}_z \quad (4.20)$$

or

$$\bar{\boldsymbol{\omega}} = -18.473\sqrt{1+0.16806 l^{-2}}\,\kappa J_1(\lambda_1\bar{r})\cos\left(\tfrac{1}{2}\pi\bar{z}/l\right)\boldsymbol{e}_r$$
$$+45.06 l\left(1+0.168\,06 l^{-2}\right)\kappa J_1(\lambda_1\bar{r})\sin\left(\tfrac{1}{2}\pi\bar{z}/l\right)\boldsymbol{e}_\theta$$
$$+18.472\,68\sqrt{1+5.9504 l^2}\,\kappa J_0(\lambda_1\bar{r})\sin\left(\tfrac{1}{2}\pi\bar{z}/l\right)\boldsymbol{e}_z. \quad (4.21)$$

Here too, based on (4.11) and (4.21), it may be straightforwardly shown that this flow is Trkalian with a configuration specific constant of $\bar{\boldsymbol{\omega}}/\bar{\boldsymbol{u}} = \lambda_1[1+\pi^2/(4\lambda_1^2 l^2)]^{1/2}$. This vorticity-to-velocity ratio remains globally fixed for a given chamber aspect ratio l.

4.2. Axially nonlinear Beltramian solution with slip

As we move to consider the slip-permitting solution, we note that only the swirl velocity distribution becomes affected by the normalized $\bar{u}_\theta(1,\bar{z}) = 1$ constraint and, by association, the vorticity, radial pressure gradient, and total pressure drop. The axial pressure gradient remains unaffected as it contains no contributions from $\bar{u}_\theta$. The dimensionless angular momentum reduces to $\bar{B} = [1+(\lambda_1^2+\frac{1}{4}\pi^2/l^2)\bar{\psi}^2]^{1/2}$ and this enables us to write

$$\bar{u}_\theta = \frac{1}{\bar{r}}\sqrt{1+c^2\kappa^2\left(\lambda_1^2 l^2+\frac{1}{4}\pi^2\right)\bar{r}^2 J_1^2(\lambda_1\bar{r})\sin^2\left(\frac{\pi\bar{z}}{2l}\right)}$$
$$= \frac{1}{\bar{r}}\sqrt{1+23.242(1+5.9504 l^2)\kappa^2\bar{r}^2 J_1^2(\lambda_1\bar{r})\sin^2\left(\frac{\pi\bar{z}}{2l}\right)}, \quad (4.22)$$

which coincides with (4.10). While the crossflow and peak radial speeds remain unchanged, the maximum tangential speed becomes unbounded in the absence of viscous damping (figure 7(d)). For the same reason, a core singularity emerges in the radial pressure gradient, which is analogous to that of (3.14). This can be seen in

$$\begin{aligned}\frac{\partial \bar{p}}{\partial \bar{r}} = \left(\frac{\partial \bar{p}}{\partial \bar{r}}\right)_{\text{noslip}} + \frac{1}{\bar{r}^3} \\ &= \bar{r}^{-3} + \frac{1}{4}c^2\kappa^2 J_1(\lambda_1\bar{r})\left\{-\pi^2\lambda_1 J_0(\lambda_1\bar{r}) + \bar{r}^{-1}J_1(\lambda_1\bar{r})\right. \\ &\quad \left.\times\left[\pi^2 + 2\lambda_1^2 l^2 - 2\lambda_1^2 l^2 \cos(\pi\bar{z}/l)\right]\right\} \\ &\approx \bar{r}^{-3} - \frac{1}{16}\pi^2 c^2\lambda_1^2\kappa^2\bar{r}\left[1 - \lambda_1^2\left(2\pi^{-2}l^2 + \frac{1}{2}\bar{r}^2\right)\right. \\ &\quad \left. + \frac{1}{2}\pi^{-2}\lambda_1^4 l^2\bar{r}^2 + 2\pi^{-2}\lambda_1^2 l^2\left(1 - \frac{1}{4}\lambda_1^2\bar{r}^2\right)\cos(\pi\bar{z}/l) + \cdots\right],\end{aligned} \tag{4.23}$$

$$\begin{aligned}\frac{\partial \bar{p}}{\partial \bar{r}} = \left(\frac{\partial \bar{p}}{\partial \bar{z}}\right)_{\text{noslip}} &= -\frac{1}{4}\pi c^2\lambda_1^2\kappa^2 l[J_0^2(\lambda_1\bar{r}) + J_1^2(\lambda_1\bar{r})]\sin(\pi\bar{z}/l) \\ &\approx -\frac{1}{4}\pi c^2\lambda_1^2\kappa^2 l\left(1 - \frac{1}{4}\bar{r}^2\lambda_1^2 + \frac{1}{32}\bar{r}^4\lambda_1^4\right)\sin(\pi\bar{z}/l) + \cdots\end{aligned} \tag{4.24}$$

and so

$$\begin{aligned}\Delta\bar{p} = (\Delta\bar{p})_{\text{noslip}} - \frac{1}{2}\bar{r}^{-2} \\ &= -\frac{1}{2}\bar{r}^{-2} - \frac{1}{8}c^2\kappa^2\left\{\pi^2 J_1^2(\lambda_1\bar{r}) + 2\lambda_1^2 l^2[J_0^2(\lambda_1\bar{r}) + J_1^2(\lambda_1\bar{r})][1 - \cos(\pi\bar{z}/l)]\right\} + \frac{1}{2} \\ &\approx -\frac{1}{2}\bar{r}^{-2} + \frac{1}{2} - \frac{1}{8}c^2\kappa^2\begin{bmatrix}2\lambda_1^2 l^2 + \frac{1}{4}\pi^2\lambda_1^2\bar{r}^2 - \frac{1}{2}\lambda_1^4 l^2\bar{r}^2 - \frac{1}{16}\pi^2\lambda_1^4\bar{r}^4 + \frac{1}{16}\lambda_1^6 l^2\bar{r}^4 \\ -2\lambda_1^2 l^2\left(1 - \frac{1}{4}\lambda_1^2\bar{r}^2 + \frac{1}{32}\lambda_1^4\bar{r}^4\right)\cos(\pi\bar{z}/l) + \cdots\end{bmatrix},\end{aligned} \tag{4.25}$$

where the recurring $\bar{r}^{-3}$ and $-\frac{1}{2}\bar{r}^{-2}$ terms in the radial pressure gradient and differential pressure drop are characteristic of free vortex behaviour. These actually coincide with their complex lamellar forms.

Finally, the vorticity for this Beltramian profile may be determined from

$$\begin{aligned}\bar{\boldsymbol{\omega}} &= \frac{-36.509(1+5.9504l^2)\kappa^2\bar{r}J_1^2(\lambda_1\bar{r})\sin(\pi\bar{z}/l)}{l\sqrt{4+92.968(1+5.9504l^2)\kappa^2\bar{r}^2 J_1^2(\lambda_1\bar{r})\sin^2\left(\frac{1}{2}\pi\bar{z}/l\right)}}\boldsymbol{e}_r \\ &\quad + \frac{7.5728(1+5.9504l^2)}{l}\kappa J_1(\lambda_1\bar{r})\sin\left(\frac{1}{2}\pi\bar{z}/l\right)\boldsymbol{e}_\theta \\ &\quad + \frac{89.057(1+5.9504l^2)\kappa^2\bar{r}J_0(\lambda_0\bar{r})J_1(\lambda_0\bar{r})[1-\cos(\pi\bar{z}/l)]}{\sqrt{4+92.968(1+5.9504l^2)\kappa^2\bar{r}^2 J_1^2(\lambda_0\bar{r})\sin^2\left(\frac{1}{2}\pi\bar{z}/l\right)}}\boldsymbol{e}_z.\end{aligned} \tag{4.26}$$

The velocity and vorticity components stemming from (4.22) and (4.26) may be readily manipulated to verify the vanishing of the Lamb vector. This may be ascribed to the

Beltramian parallelism caused by

$$\frac{\bar{\boldsymbol{\omega}}}{\bar{\boldsymbol{u}}} = \lambda_1 \left[1 + \frac{\pi^2}{4\lambda_1^2 l^2} + \frac{1}{c^2\kappa^2\lambda_1^2 l^2 \bar{r}^2 \sin^2\left(\frac{1}{2}\pi\bar{z}/l\right) J_1^2(\lambda_1 \bar{r})} \right]^{-1/2}. \tag{4.27}$$

So while $\bar{\boldsymbol{\omega}}$ and $\bar{\boldsymbol{u}}$ retain a fixed relative alignment throughout the chamber, the ratio of relative magnitudes $|\bar{\boldsymbol{\omega}}/\bar{\boldsymbol{u}}|$ varies locally from one point to the other. This feature is, of course, characteristic of a Beltramian field. Another distinct property that all of the new models exhibit may be encapsulated by the vector relation $\bar{\boldsymbol{\omega}}/\bar{\boldsymbol{u}} = \bar{B}/\bar{\psi}$. Accordingly, the vorticity-to-velocity ratio remains everywhere identical to the ratio of the tangential angular momentum and the stream function.

In the interest of clarity, a summary of the main equations associated with the axially nonlinear solutions is posted in table 4. The character of the vorticity is illustrated in figure 9 for the two models at hand, using both radial vorticity lines at fixed $\bar{z}$ (in (a), (c)) and isovorticity contours in the $\bar{r}-\bar{z}$ plane (in (b), (d)). These plots may also be compared to those given in figure 5 for the $\upsilon = 0$ cases.

Consistently with the velocity and pressure attributes, we find these axially nonlinear helical profiles to produce higher levels of vorticity magnitudes and spatial distributions that are specifically connected to their core vortex evolution. In figures 9(a) and (b), it is clear that $\bar{\omega}$ approaches a constant value as $\bar{r} \to 0$. The constant angular rotation of the fluid near the centreline is reassuring, being characteristic of forced vortex motion. It can be seen not only in figures 9(a) and (b) but also, in figures 5(a) and (b) where the corresponding swirl velocity vanishes at the radial endpoints. In contrast, the trends in figures 9(c) and (d) bear a striking resemblance, despite having slightly higher magnitudes than those depicted in figures 5(c) and (d). These slip permitting Beltramian profiles give rise to an irrotational region near the chamber axis where, in practice, viscous stresses become prevalent. A similar irrotational region appears near the wall where the velocity adherence condition is relaxed. Thus, given the rich characteristics that the Beltramian profiles exhibit in comparison to the complex lamellar model, it may be safely argued that this new class of inviscid profiles stands to provide useful approximations for the swirl induced bidirectional motions, especially when their viscous boundary layers are accounted for.

4.3. Three-dimensional flow representation

Before leaving this section, a three-dimensional comparison is provided between the complex lamellar solution with wall slip and both linear and nonlinear Beltramian models at several values of κ. This is accomplished in figure 10 where vector plots of the three profiles at hand are depicted while varying κ over three orders of magnitude, starting at the top with a value of unity. As one would expect for $\kappa = 1$, the contributions of the off-swirl velocity components $\bar{u}_r$ and $\bar{u}_z$ become essentially identical to those of $\bar{u}_\theta$. The resulting behaviour is reflected in the top row of figure 10 where the effects of axial and radial transport can be clearly discerned in all three models. In this configuration, the flow enters the right-cylindrical chamber from the top annular section, spirals downwardly, reverses direction at the headwall, and then sweeps upwardly while revolving around the chamber axis. Using this basic case as a benchmark, the intensification of swirl can be captured in the second and third rows where the relative contributions of $\bar{u}_r$ and $\bar{u}_z$ are deliberately diminished by two orders of magnitude, i.e., by reducing κ first to 0.1, and then to 0.01. For the smallest value of κ, the influence of axial and radial motions can be hardly discerned as the flow becomes noticeably swirl dominated.

Despite the three distinct mathematical representations of the profiles in question, their three-dimensional vector plots furnished in figure 10 exhibit strong graphical similarities.

Table 4. Beltramian and Trkalian cases with $\upsilon = \frac{1}{2}\pi/L$.

Variable	Equation
	Common parts
$\bar{\psi}$	$c\kappa l\, \bar{r} \sin\left(\frac{1}{2}\pi \bar{z}/l\right) J_1(\lambda_1 \bar{r})$
$(\bar{u}_r)_{\text{cross}}$	$-2.5028\kappa \cos\left(\frac{1}{2}\pi \bar{z}/l\right)$
$(\bar{u}_r)_{\text{min}}$	$-2.8052\kappa \cos\left(\frac{1}{2}\pi \bar{z}/l\right)$
$\dfrac{\partial \bar{p}}{\partial \bar{z}}$	$-\frac{1}{4}\pi c^2 \lambda_1^2 \kappa^2 l [J_0^2(\lambda_1 \bar{r}) + J_1^2(\lambda_1 \bar{r})] \sin(\pi \bar{z}/l)$
	Trkalian case with no slip
$\bar{\boldsymbol{u}}$	$\begin{cases} -\frac{1}{2}\pi c\kappa \cos\left(\frac{1}{2}\pi \bar{z}/l\right) J_1(\lambda_1 \bar{r})\, \boldsymbol{e}_r + c\lambda_1 \kappa l \sin\left(\frac{1}{2}\pi \bar{z}/l\right) J_0(\lambda_1 \bar{r})\, \boldsymbol{e}_z \\ +\frac{1}{2}\pi c\kappa \sqrt{1 + 4\lambda_1^2 l^2/\pi^2} \sin\left(\frac{1}{2}\pi \bar{z}/l\right) J_1(\lambda_1 \bar{r})\, \boldsymbol{e}_\theta \end{cases}$
$\bar{\boldsymbol{\omega}}$	$\begin{cases} -\frac{1}{2}c\pi\kappa \sqrt{\lambda_1^2 + \frac{1}{4}\pi^2/l^2} J_1(\lambda_1 \bar{r}) \cos\left(\frac{1}{2}\pi \bar{z}/l\right) \boldsymbol{e}_r + c\kappa l (\lambda_1^2 + \frac{1}{4}\pi^2/l^2) J_1(\lambda_1 \bar{r}) \sin\left(\frac{1}{2}\pi \bar{z}/l\right) \boldsymbol{e}_\theta \\ + c\kappa l \lambda_1 \sqrt{\lambda_1^2 + \frac{1}{4}\pi^2/l^2} J_0(\lambda_1 \bar{r}) \sin\left(\frac{1}{2}\pi \bar{z}/l\right) \boldsymbol{e}_z \end{cases}$
$(\bar{u}_\theta)_{\text{max}}$	$0.4465\sigma^{-1}\sqrt{l^{-2} + 5.9504} \sin\left(\frac{1}{2}\pi \bar{z}/l\right)$
$\dfrac{\partial \bar{p}}{\partial \bar{r}}$	$\frac{1}{4}c^2\kappa^2 J_1(\lambda_1 \bar{r}) \left\{-\pi^2 \lambda_1 J_0(\lambda_1 \bar{r}) + \bar{r}^{-1} J_1(\lambda_1 \bar{r}) \left[\pi^2 + 2l^2\lambda_1^2 - 2l^2\lambda_1^2 \cos(\pi \bar{z}/l)\right]\right\}$
$\Delta \bar{p}$	$-\frac{1}{8}c^2\kappa^2 \left\{\pi^2 J_1^2(\lambda_1 \bar{r}) + 2\lambda_1^2 l^2 [J_0^2(\lambda_1 \bar{r}) + J_1^2(\lambda_1 \bar{r})] [1 - \cos(\pi \bar{z}/l)]\right\}$
$\tilde{\Omega}$	$\frac{1}{48}\beta\lambda_1^2 \sqrt{4\lambda_1^2 + \pi^2/l^2}\, {}_2F_3\left[\left(\frac{3}{2}, \frac{3}{2}\right), \left(2, 2, \frac{5}{2}\right), -\beta^2\lambda_1^2\right] J_1^{-2}(\beta\lambda_1) \approx 0.549\,604\sqrt{1 + 5.9504 l^2}$
	Beltramian case with slip
$\bar{\boldsymbol{u}}$	$\begin{cases} -\frac{1}{2}\pi c\kappa \cos\left(\frac{1}{2}\pi \bar{z}/l\right) J_1(\lambda_1 \bar{r})\, \boldsymbol{e}_r + c\lambda_1 \kappa l \sin\left(\frac{1}{2}\pi \bar{z}/l\right) J_0(\lambda_1 \bar{r})\, \boldsymbol{e}_z \\ +\frac{1}{\bar{r}} \sqrt{1 + c^2\kappa^2 \left(\lambda_1^2 l^2 + \frac{1}{4}\pi^2\right) \bar{r}^2 J_1^2(\lambda_1 \bar{r}) \sin^2\left(\frac{1}{2}\pi \bar{z}/l\right)} \boldsymbol{e}_\theta \end{cases}$
$\bar{\boldsymbol{\omega}}$	$\begin{cases} -\dfrac{c^2\pi\kappa^2(\pi^2 + 4l^2\lambda_1^2)\bar{r} J_1^2(\lambda_1 \bar{r}) \sin(\pi \bar{z}/l)}{8l\sqrt{4 + c^2\kappa^2(\pi^2 + 4l^2\lambda_1^2)\bar{r}^2 J_1^2(\lambda_1 \bar{r}) \sin^2\left(\frac{1}{2}\pi \bar{z}/l\right)}} \boldsymbol{e}_r + \dfrac{c\kappa}{4l}(\pi^2 + 4l^2\lambda_1^2) J_1(\lambda_1 \bar{r}) \sin\left(\frac{1}{2}\pi \bar{z}/l\right) \boldsymbol{e}_\theta \\ + \dfrac{c^2\lambda_1\kappa^2(\pi^2 + 4l^2\lambda_1^2)\bar{r} J_0(\lambda_1 \bar{r}) J_1(\lambda_1 \bar{r}) [1 - \cos(\pi \bar{z}/l)]}{4\sqrt{4 + c^2\kappa^2(\pi^2 + 4l^2\lambda_1^2)\bar{r}^2 J_1^2(\lambda_1 \bar{r}) \sin^2\left(\frac{1}{2}\pi \bar{z}/l\right)}} \boldsymbol{e}_z \end{cases}$
$(\bar{u}_\theta)_{\text{max}}$	∞
$\dfrac{\partial \bar{p}}{\partial \bar{r}}$	$\bar{r}^{-3} + \frac{1}{4}c^2\kappa^2 J_1(\lambda_1 \bar{r}) \left\{-\pi^2 \lambda_1 J_0(\lambda_1 \bar{r}) + \bar{r}^{-1} J_1(\lambda_1 \bar{r}) \left[\pi^2 + 2l^2\lambda_1^2 - 2l^2\lambda_1^2 \cos(\pi \bar{z}/l)\right]\right\}$
$\Delta \bar{p}$	$-\frac{1}{2}\bar{r}^{-2} - \frac{1}{8}c^2\kappa^2 \left\{\pi^2 J_1^2(\lambda_1 \bar{r}) + 2\lambda_1^2 l^2 [J_0^2(\lambda_1 \bar{r}) + J_1^2(\lambda_1 \bar{r})] [1 - \cos(\pi \bar{z}/l)]\right\} + \frac{1}{2}$

To better understand their differences, it is helpful to fix κ and showcase their unique flow features by taking horizontal cuts at several equispaced vertical stations along the length of the chamber. These polar slices are given in figure 11 for $\kappa = 1$ and, from top to bottom, $z/L = 0.25, 0.5, 0.75$, and 1. By maintaining a constant value of κ in any given row, it may

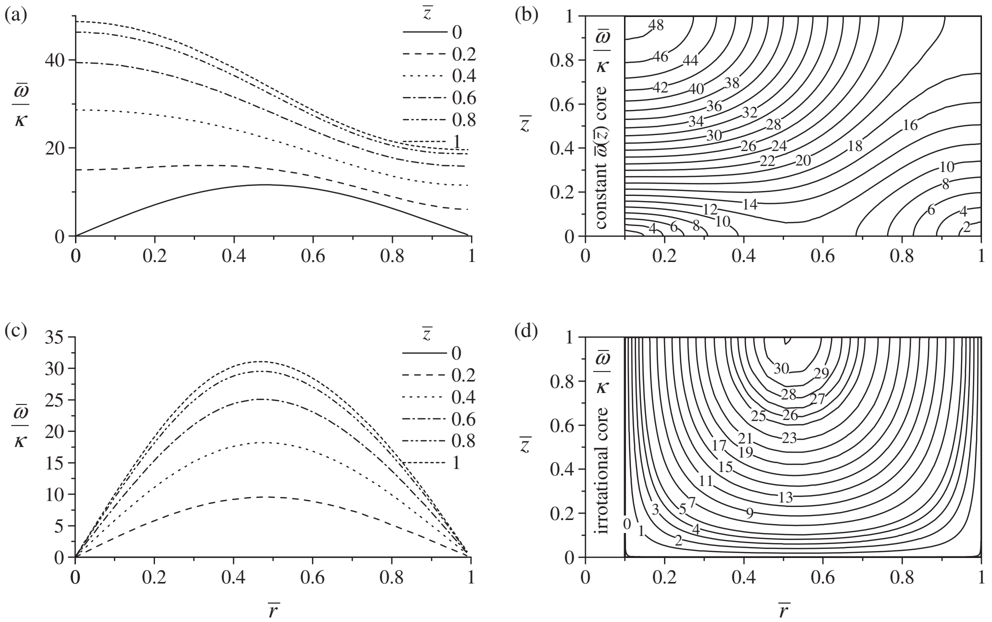

Figure 9. Radial distribution of total vorticity along (a) fixed axial positions and (b) isolines. The same is repeated in (c) and (d) for the slip permitting Beltramian solution.

be seen that the role of axial and radial transport becomes less appreciable from left to right, and from top to bottom, as the endwall station is approached. In comparison to the complex lamellar solution, the effect of swirl on the linear and nonlinear Beltramian profiles tends to be more pronounced, especially in the aft sections of the chamber. Also consistent with equation (4.4), it may be seen that the nonlinear Beltramian case corresponding to $z = L$ constitutes a limiting configuration with no radial flow.

5. Solutions with sidewall injection

5.1. Extended boundary conditions

The solutions presented heretofore can be modified to the extent of accounting for sidewall mass injection. Such a problem arises in the modelling of hybrid rocket internal gas dynamics. The so-called VIHRE represents one such example in which wall blowing is induced by the inward ejection of gases into a bidirectional vortex flow field. The original VIHRE problem was analysed assuming complex lamellar base flow motion by Majdalani (2007). The main departure from the hardwall problem lies in prescribing a surface boundary condition that captures the effects of sidewall mass addition. This is achieved by replacing (2.9*c*) by $u_r(a, z) = -U_\mathrm{w}$, where U_w denotes the effective blowing speed at the sidewall. Moreover, the expression for mass conservation may be expanded to account for the secondary wall influx. This can be accomplished by setting

$$\int_0^{2\pi}\int_0^b \boldsymbol{u}(r, L)\cdot\boldsymbol{n}r\,\mathrm{d}r\,\mathrm{d}\theta = 2\pi\int_0^b u_z(r, L)\,r\,\mathrm{d}r = Q_\mathrm{in} = Q_i + Q_\mathrm{w} = UA_i + 2\pi aLU_\mathrm{w}. \tag{5.1}$$

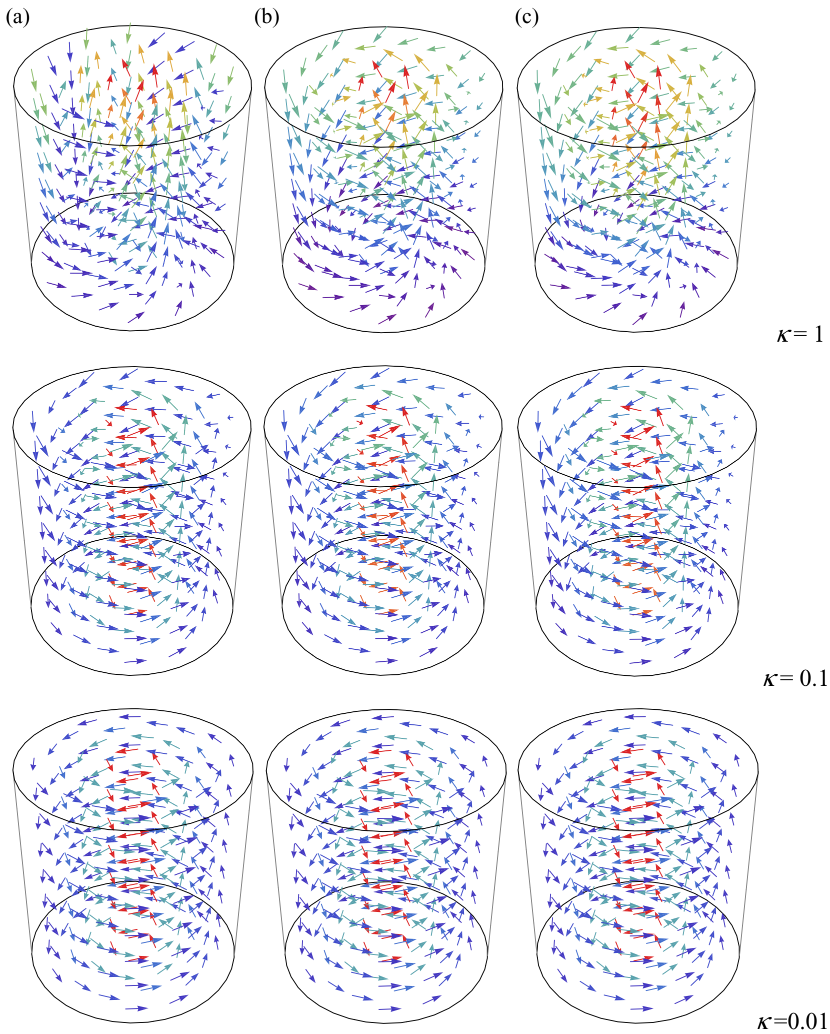

Figure 10. Three-dimensional vector plots of the three fundamental helical profiles corresponding to (a) complex lamellar, (b) $\upsilon = 0$ (linear Beltramian), and (c) $\upsilon = \frac{1}{2}\pi/L$ (nonlinear Beltramian) motions. Here $l = 2$ and, from top down, $\kappa = 1$, 0.1, and 0.01, thus depicting three distinct orders of magnitude in swirl intensity.

The first two boundary conditions in (2.9*a*) and (2.9*b*) act to suppress axial transport at the headwall and radial motion across the centreline. They may be employed to transform (2.8) into

$$\psi(r, z) = \begin{cases} \psi_0 z r J_1(rC), & \upsilon = 0, \quad (a) \\ \\ \psi_0 r \sin(\upsilon z) J_1(r\sqrt{C^2 - \upsilon^2}), & \upsilon^2 < C^2, \quad (b) \end{cases} \tag{5.2}$$

where the hypergeometric form is deliberately ignored, while the remaining solutions are denoted by (a) and (b), sequentially. To make further headway, global conservation

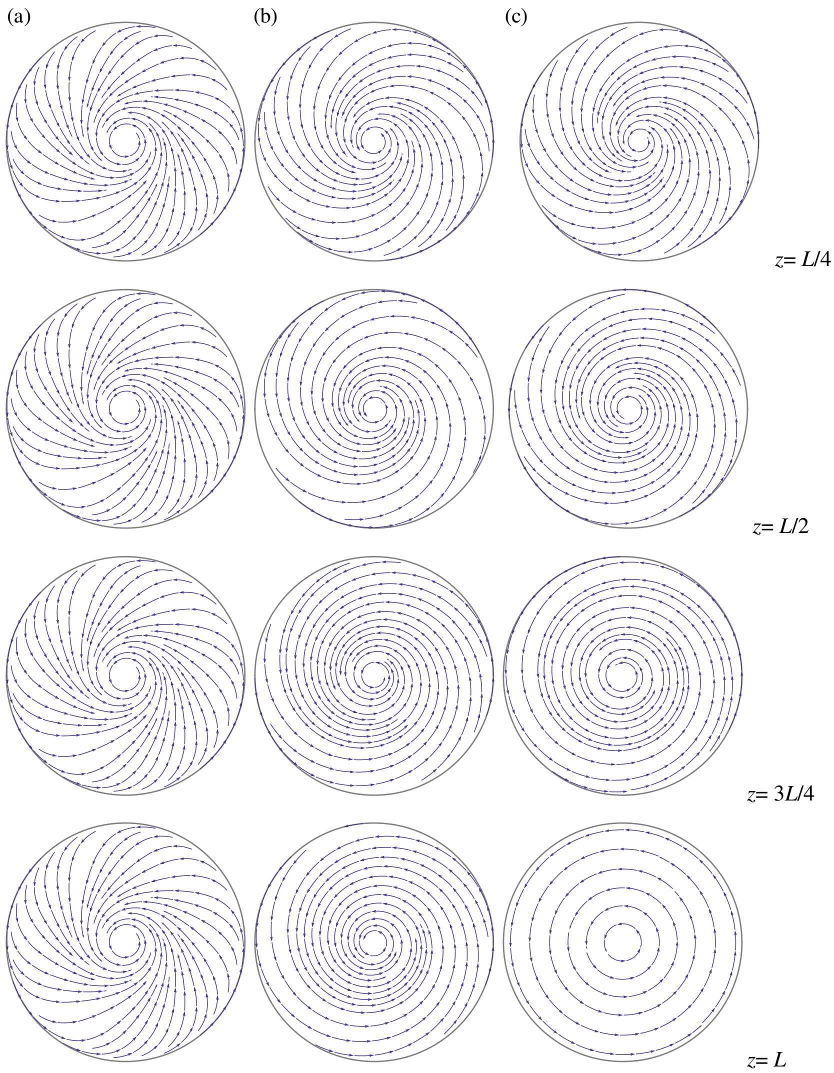

Figure 11. Streamline plots taken in a planar $r-\theta$ section of the three fundamental helical profiles corresponding to (a) complex lamellar, (b) $\upsilon=0$ (linear Beltramian), and (c) $\upsilon=\frac{1}{2}\pi/L$ (nonlinear Beltramian) motions. Here $\kappa=1$, $l=2$, and, from top down, $z/L=0.25$, 0.5, 0.75, and 1, thus depicting characteristic variations in the radial and tangential velocity contributions at several axial stations.

through (5.1) may be enforced to the point of retrieving

$$\psi_0=\begin{cases}\dfrac{Q_{\text{in}}}{2\pi a\beta L J_1(bC)}, & (a)\\[2ex] \dfrac{Q_{\text{in}}}{2\pi a\beta J_1\left(b\sqrt{C^2-\frac{1}{4}\pi^2/L^2}\right)}. & (b)\end{cases} \tag{5.3}$$

Subsequently, in order to satisfy the spatially uniform constraint $u_r(a, z) = -U_\mathrm{w}$, it is necessary to set

$$\begin{cases} \psi_0 J_1(Ca) = U_\mathrm{w}, & (a) \\ \psi_0 \upsilon \cos(\upsilon z) J_1(a\sqrt{C^2 - \upsilon^2}) = U_\mathrm{w}. & (b) \end{cases} \tag{5.4}$$

Note that the second member of (5.4) cannot be secured unless the blowing velocity is cosine harmonic, namely of the form $u_r(a, z) = -U_\mathrm{w}\cos(\upsilon z)$. Then given the endwall assumption, $u_r(r, L) = 0$, one deduces the necessity of selecting $\upsilon = \frac{1}{2}\pi/L$. A solution for a wall injection distribution of $u_r(a, z) = -U_\mathrm{w}\cos(\frac{1}{2}\pi z/L)$ can therefore be accommodated by the axially nonlinear profile. The contiguous pair of wall conditions, which seem appropriate of this problem, may be written as

$$u_r(a, z) = \begin{cases} -U_\mathrm{w}, & \upsilon = 0, \quad (a) \\ -U_\mathrm{w}\cos\left(\frac{1}{2}\pi z/L\right), & \upsilon = \frac{1}{2}\pi/L. \quad (b) \end{cases} \tag{5.5}$$

Evidently, other forms of wall injection patterns may be prescribed but these are not considered here.

5.2. *Stream function formulation*

Imposing (5.5) leads to

$$\begin{cases} \dfrac{Q_\mathrm{in}}{2\pi bL}\dfrac{J_1(aC)}{J_1\,(bC)} = U_\mathrm{w}, & (a) \\ \dfrac{Q_\mathrm{in}}{4bL}\dfrac{J_1(a\sqrt{C^2 - \frac{1}{4}\pi^2/L^2})}{J_1\left(b\sqrt{C^2 - \frac{1}{4}\pi^2/L^2}\right)} = U_\mathrm{w}. & (b) \end{cases} \tag{5.6}$$

These can be expanded using

$$\begin{cases} \dfrac{Q_i + 2\pi aLU_\mathrm{w}}{2\pi bL}\dfrac{J_1(aC)}{J_1\,(bC)} = U_\mathrm{w}, \\ \dfrac{Q_i + 2\pi aLU_\mathrm{w}}{4bL}\dfrac{J_1(a\sqrt{C^2 - \frac{1}{4}\pi^2/L^2})}{J_1\left(b\sqrt{C^2 - \frac{1}{4}\pi^2/L^2}\right)} = U_\mathrm{w} \end{cases}$$

$$\text{or} \quad \begin{cases} (\kappa U + U_\mathrm{w})\dfrac{J_1(aC)}{\beta J_1\,(bC)} = U_\mathrm{w}, \\ \dfrac{\pi}{2}\,(\kappa U + U_\mathrm{w})\dfrac{J_1(a\sqrt{C^2 - \frac{1}{4}\pi^2/L^2})}{\beta J_1\left(b\sqrt{C^2 - \frac{1}{4}\pi^2/L^2}\right)} = U_\mathrm{w}, \end{cases} \tag{5.7}$$

where group parameters leading to κ and β have been combined. The emergence of the characteristic velocities in the right-hand-side expressions prompts us to divide through by

U and rearrange. Then using $\varepsilon = U_w/U$, we are left with

$$\begin{cases} \dfrac{J_1(aC)}{J_1(bC)} = \dfrac{\varepsilon\beta}{\kappa+\varepsilon}, & (a) \\[2ex] \dfrac{J_1(a\sqrt{C^2-\frac{1}{4}\pi^2/L^2})}{J_1\left(b\sqrt{C^2-\frac{1}{4}\pi^2/L^2}\right)} = \dfrac{2}{\pi}\dfrac{\varepsilon\beta}{\kappa+\varepsilon} & (b) \end{cases}$$

$$\text{or}\quad \frac{J_1(\lambda_m)}{J_1(\beta\lambda_m)} = \begin{cases} \dfrac{\varepsilon\beta}{\kappa+\varepsilon}, & C_m = \dfrac{\lambda_m}{a}, & (a) \\[2ex] \dfrac{2}{\pi}\dfrac{\varepsilon\beta}{\kappa+\varepsilon}, & C_m = \sqrt{\dfrac{\lambda_m^2}{a^2}+\dfrac{\pi^2}{4L^2}}. & (b) \end{cases} \tag{5.8}$$

This last expression enables us to identify multiple solutions for λ_m at fixed open fraction β, sidewall injection ratio ε, and tangential inflow parameter κ. Using λ_1 to specify the lowest root of (5.8), which one may associate with the development of a single mantle, it is possible to numerically obtain the universe of solutions $\lambda_1 = \lambda_1(\beta, \varepsilon, \kappa)$ directly from

$$\frac{J_1(\lambda_1)}{J_1(\beta\lambda_1)} = \left\{ \frac{\varepsilon\beta}{\kappa+\varepsilon},\quad C_1 = \frac{\lambda_1}{a}\quad (a),\quad \frac{2}{\pi}\frac{\varepsilon\beta}{\kappa+\varepsilon},\quad C_1 = \sqrt{\frac{\lambda_1^2}{a^2}+\frac{\pi^2}{4L^2}},\quad (b) \right\} \tag{5.9}$$

where β depends on the relative size of the geometric outlet. The resulting stream function becomes

$$\psi(r,z) = \begin{cases} \dfrac{Q_{\text{in}}}{2\pi a\beta L J_1(\beta\lambda_1)} zr J_1\left(\dfrac{\lambda_1 r}{a}\right) = \dfrac{\kappa U + U_w}{\beta J_1(\beta\lambda_1)} rz J_1\left(\dfrac{\lambda_1 r}{a}\right), & (a) \\[2ex] \dfrac{Q_{\text{in}}}{2\pi a\beta J_1(\beta\lambda_1)} r \sin\left(\dfrac{\pi z}{2L}\right) J_1\left(\dfrac{\lambda_1 r}{a}\right) = \dfrac{\kappa U + U_w}{\beta J_1(\beta\lambda_1)} rL \sin\left(\dfrac{\pi z}{2L}\right) J_1\left(\dfrac{\lambda_1 r}{a}\right) & (b) \end{cases} \tag{5.10}$$

and so, in dimensionless form,

$$\bar\psi(\bar r,\bar z) = \begin{cases} \dfrac{\kappa+\varepsilon}{\beta J_1(\beta\lambda_1)} \bar r\bar z J_1(\lambda_1\bar r), & (a) \\[2ex] \dfrac{\kappa+\varepsilon}{\beta J_1(\beta\lambda_1)} \bar r l \sin\left(\dfrac{\pi\bar z}{2l}\right) J_1(\lambda_1\bar r) & (b) \end{cases}$$

$$\text{or}\quad \bar\psi(\bar r,\bar z) = \begin{cases} c\kappa_\varepsilon \bar r\bar z J_1(\lambda_1\bar r), & (a) \\[2ex] c\kappa_\varepsilon \bar r l \sin\left(\frac{1}{2}\pi\bar z/l\right) J_1(\lambda_1\bar r), & (b) \end{cases} \tag{5.11}$$

$$\text{where}\quad \kappa_\varepsilon \equiv \kappa+\varepsilon \quad\text{and}\quad c \equiv 1/[\beta J_1(\beta\lambda_1)]. \tag{5.12}$$

In view of the perfect similarity that stands between (5.11) and the stream functions with no sidewall injection, the key formulations for the various cases that may be explored need not

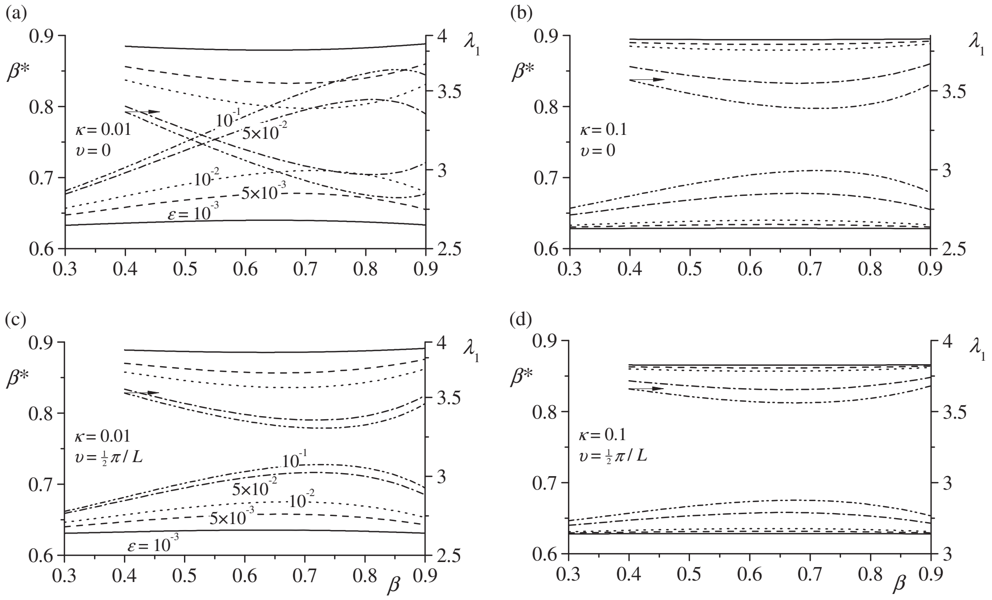

Figure 12. Variation of the mantle location β^* and corresponding eigenvalue λ_1 as function of the chamber's open fraction β. Results are shown for several values of the sidewall injection ratio ϵ and two fixed values of the tangential inflow parameter κ.

be re-derived. Their final outcome may be arrived at directly by replacing the impermeable κ by κ_ε. The other difference consists of allowing λ_1 and β^* to vary as per (5.9).

5.3. Mantle sensitivity to sidewall injection, open outlet fraction, and inflow parameter

The mantle with wall blowing may be located, just as usual, by setting $\bar{u}_z(\beta^*, \bar{z}) = 0$. This equality translates into

$$J_0\left(\lambda_1\beta^*\right) = 0 \quad \text{or} \quad \beta^* = \frac{j_0}{\lambda_1} = \frac{2.404\,825\,56}{\lambda_1}, \tag{5.13}$$

where j_0 is the appropriate root of $J_0(j_0) = 0$. In general, given a design specific β, λ_1 may be computed from (5.9) at fixed ε and κ, and then inserted into (5.13) to deduce the mantle location. For example, when conditions correspond to $\beta = 0.7$, $\varepsilon = 0.01$ and $\kappa = 0.125$, one calculates, for $\upsilon = 0$, $\lambda_1 = 3.773\,02$, and $\beta^* = 0.637\,375$. The same analysis for $\upsilon = \frac{1}{2}\pi/L$ yields a slightly higher eigenvalue of $\lambda_1 = 3.794\,61$, and a lower value of $\beta^* = 0.633\,748$.

The mantle's dependence on β, ε, λ_1, κ, and υ, is illustrated in figure 12 where variations in both β^* (left scale) and λ_1 (right scale) are depicted versus β. Results are shown along five constant sidewall injection lines corresponding to $\varepsilon = 10^{-3}$, 5×10^{-3}, 10^{-2}, 5×10^{-2}, and 10^{-1} using (a) $\kappa = 0.01$, $\upsilon = 0$, (b) $\kappa = 0.1$, $\upsilon = 0$, (c) $\kappa = 0.01$, $\upsilon = \frac{1}{2}\pi/L$, and (d) $\kappa = 0.1$, $\upsilon = \frac{1}{2}\pi/L$. At the outset, it may be inferred that increasing κ relative to ε reduces the variability of the mantle location. This can be attributed to the asymptotic nature of the right-hand-side of (5.9). Conversely, increasing ε leads to a heightened sensitivity of β^* to small variations in β. Common to all four cases shown, β^* first increases with β, reaches a peak value at $\beta = \beta^*$, and then falls off with further increases in the open outlet fraction. For $\varepsilon \leqslant 10^{-4}$ (not shown) a flattening of the β and λ_1 curves occurs as the solution levels off to the

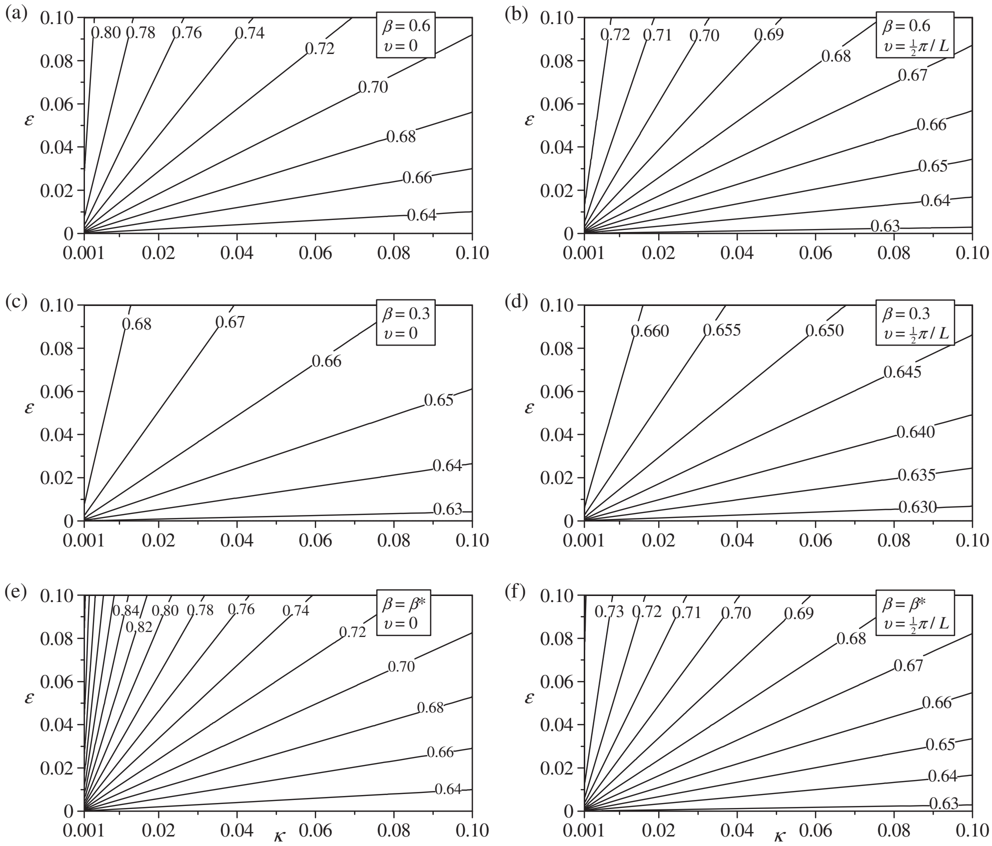

Figure 13. Iso-parametric variation of the mantle position β^* with ε and κ given (a), (b) $\beta = 0.6$, (c), (d) $\beta = 0.3$, and (e), (f) $\beta = \beta^*$.

constant mantle location associated with the no injection (hardwall) configuration. We hence recover flat lines at $\beta^* = 0.627\,612$ and $\lambda_1 = 3.8317$.

To further elucidate the mantle's variability with the tangential inflow and sidewall injection parameters, contour plots of constant β^* are provided in figure 13 for the two cases in question. This parametric study is performed over a wide range of ε and κ, albeit at fixed values of the open outlet fraction, $\beta = 0.6$ (a, b), $\beta = 0.3$ (c, d), and $\beta = \beta^*$ (e, f). Nonetheless, the results for the (a)–(d) cases remain characteristic of a typical geometric opening β. They clearly show that: (i) increasing either ε at constant κ leads to an outward shift in the mantle; (ii) decreasing κ (i.e. increasing swirl) at constant ε leads to an outward shift in the mantle; (iii) at any fixed ε or κ, $\beta^*_{\upsilon=0} > \beta^*_{\upsilon=\frac{1}{2}\pi/L}$; and (iv) constricting the geometric opening β plays an appreciable role in reducing the sensitivity of the mantle to inlet and sidewall injection levels.

Graphically, it may be surmised that the excursion range of β^* is considerably diminished when β is decreased. The converse is true in that the variability of β^* is expanded, at least in theory, when the outlet opening is progressively enlarged. On this note, it may be instructive to recall that several other investigators have reported similar shifting in mantle positioning due to geometric modifications influencing their outlets. In the context of cyclone separators, the experimental bias caused by changing the diameter of the vortex finder has been widely reported in the literature (Hsieh and Rajamani 1991, Hoekstra *et al* 1998, 1999, Derksen and van den Akker 2000). This behaviour is also alluded to in the classic work by Smith (1962a, 1962b) cited earlier in this study.

In the interest of simplicity, one may set $\beta = \beta^*$, thus envisioning a geometric outlet radius that tracks and matches the mantle's radius (cf Majdalani 2007). This notion was introduced with the intent of eliminating irregularities that may arise at $z = L$, such as collisions and recirculatory cells. The same idealization leads to a fluid dynamically consistent model in which the axial annular flow sweeping towards the headwall from positive infinity (i.e., the axial source at $z = L$) can naturally reverse direction and return unencumbered, through the inner vortex region, to positive infinity. By setting $\beta = \beta^*$, we are effectively ensuring that the diameter of the inner vortex matches the diameter of the open boundary at $z = L$. We are also capturing the peak values reported in figure 12. For this hypothetical setting, (5.9) reduces to:

$$\beta = \beta^* = \frac{j_0}{\lambda_1}, \quad \frac{\lambda_1 J_1(\lambda_1)}{j_0 J_1(j_0)} = \begin{cases} \dfrac{\varepsilon}{\kappa + \varepsilon}, & (a) \\ \dfrac{2}{\pi}\dfrac{\varepsilon}{\kappa + \varepsilon}. & (b) \end{cases} \tag{5.14}$$

Figures 13(e) and (f) display the contours of β^* over a full range of ε and κ. In comparison to the previously featured cases of figures 13(a)–(d), the mantle offset is not only the largest of the group but also the most widespread. Here too, we confirm that $\beta^*_{\upsilon=0} > \beta^*_{\upsilon=\frac{1}{2}\pi/L}$.

In addition to the $\beta = \beta^*$ configuration, a practical scenario that is worth investigating consists of fixing the outlet radius to a design-specific value. In the absence of user input, the logical choice would be to set $\beta = 0.6276$, being the lowest β^* that the mantle will tolerate in the limit of $\varepsilon \to 0$. In either configurations, solutions may be obtained straightforwardly from (5.11).

5.4. Other characteristic properties

Despite the mantle's parametric sensitivity, the crossflow velocity can be readily obtained from

$$(\bar{u}_r)_{\text{cross}} = \begin{cases} -\kappa_\varepsilon \dfrac{J_1(\lambda_1 \beta^*)}{\beta J_1(\beta\lambda_1)}, & (a) \\ -\dfrac{1}{2}\pi\kappa_\varepsilon \cos\left(\dfrac{1}{2}\pi\bar{z}/l\right) \dfrac{J_1(\lambda_1\beta^*)}{\beta J_1(\beta\lambda_1)}. & (b) \end{cases} \tag{5.15}$$

Due to the axial invariance of (5.15*a*), its behaviour may be captured in figure 14(a), albeit at a single value of κ. Interestingly, the crossflow is substantially increased when the outlet fraction is lowered. In fact, $(\bar{u}_r)_{\text{cross}}$ becomes very weakly dependent on ε for approximately $\beta < 0.55$. By way of comparison, the axially nonlinear solution is featured in figures 14(b)–(d) where its axial variation is characterized. Here too, reducing the outlet fraction is seen to induce an increase in the absolute magnitude of the crossflow along the mantle. For the ideal case of $\beta = \beta^*$, (5.15) reduces to

$$\frac{(\bar{u}_r)_{\text{cross}}}{\kappa_\varepsilon} = \begin{cases} -\dfrac{1}{\beta}, & (a) \\ -\dfrac{\pi}{2\beta}\cos\left(\dfrac{1}{2}\pi\bar{z}/l\right). & (b) \end{cases} \tag{5.16}$$

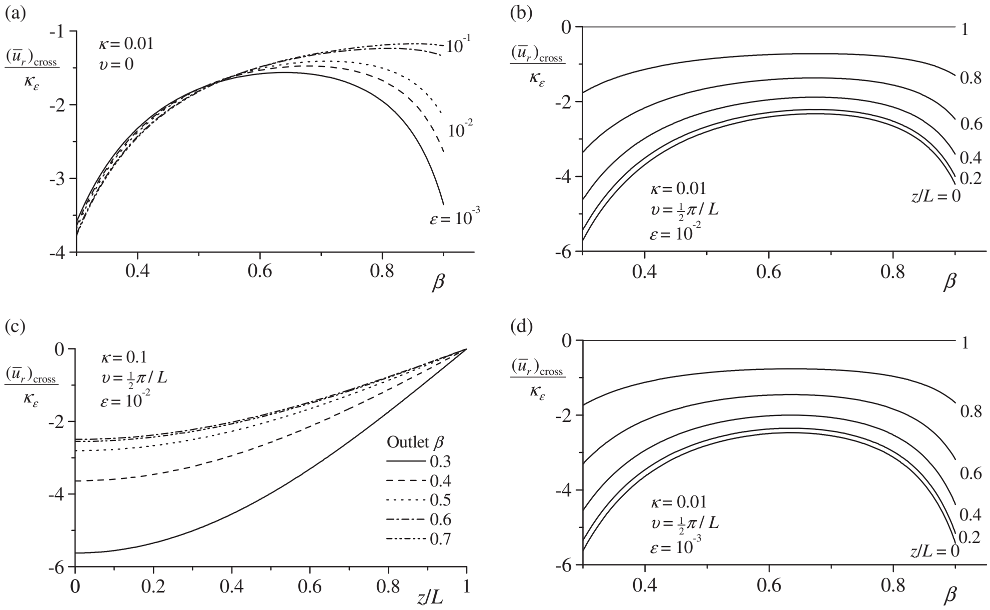

Figure 14. Variation of the crossflow velocity with β and ϵ. While the case of $\upsilon = 0$ is featured in (a), parts (b)–(d) correspond to the $\upsilon = \frac{1}{2}\pi/L$ solution.

Equation (5.16) reminds us of the expressions provided in tables 3 and 4 in which the crossflow velocity for the no-wall injection case are listed. Those entries may be recovered from (5.16) by replacing κ_ε with κ while letting $\beta = 0.627\,612$. The converse is true of other characteristic flow attributes by virtue of the parental role that the stream function plays in (5.11). To avoid duplicating steps that have been thoroughly outlined in previous sections, a summary of the key features of the bidirectional vortex with sidewall injection is furnished in tables 5 and 6. In forthcoming work, most of these features will be used as outer approximations in the context of a boundary layer treatment that seeks to overcome the intransigent singularities and limitations of an inviscid fluid. Additionally, an asymptotic approach will be presented as an alternate avenue for capturing the secondary effects of sidewall injection.

6. Conclusions

In this study, the BHE is used as a starting point to identify new inviscid models of the bidirectional vortex in a right-cylindrical chamber with and without sidewall injection. Our work constitutes a crucial extension to existing studies leading to complex lamellar models of cyclonic flows. By granting the tangential angular momentum the freedom to vary with the stream function, several helical solutions are developed under steady, inviscid, rotational and incompressible fluid conditions for which the total pressure remains invariant along streamlines. In such an isentropic environment, two families of solutions are identified, namely, Trkalian and Beltramian, with either linear or nonlinear axial sensitivities. Our formulations are compared to one another and to a complex lamellar model obtained through the use of the vorticity-stream function approach. Despite common features that these solutions share, they still exhibit fundamental differences. These affect their minima

Table 5. Beltramian and Trkalian cases with sidewall injection and $\upsilon = 0$.

Variable	Equation
	Common parts
$\bar{\psi}$	$c\kappa_\varepsilon \bar{z}\,\bar{r} J_1(\lambda_1 \bar{r})$
$\bar{u}_r$	$-c\kappa_\varepsilon J_1\,(\lambda_1 \bar{r})$
$\bar{u}_z$	$c\lambda_1 \kappa_\varepsilon \bar{z} J_0\,(\lambda_1 \bar{r})$
$\dfrac{\partial \bar{p}}{\partial \bar{z}}$	$-c^2\lambda_1^2\kappa_\varepsilon^2 \bar{z}[J_0^2(\lambda_1\bar{r}) + J_1^2(\lambda_1\bar{r})]$
	Trkalian case with no slip
$\bar{u}_\theta$	$c\lambda_1\kappa_\varepsilon \bar{z} J_1\,(\lambda_1\bar{r})$
$\bar{\boldsymbol{\omega}}$	$-c\lambda_1\kappa_\varepsilon J_1\,(\lambda_1\bar{r})\,\boldsymbol{e}_r + c\lambda_1^2\kappa_\varepsilon\bar{z}J_1\,(\lambda_1\bar{r})\,\boldsymbol{e}_\theta + c\lambda_1^2\kappa_\varepsilon\bar{z}J_0\,(\lambda_1\bar{r})\,\boldsymbol{e}_z$
$\dfrac{\partial \bar{p}}{\partial \bar{r}}$	$c^2\kappa_\varepsilon^2\left[(1+\lambda_1^2\bar{z}^2)\bar{r}^{-1}J_1^2(\lambda_1\bar{r}) - \lambda_1 J_1(\lambda_1\bar{r})J_0(\lambda_1\bar{r})\right]$
$\Delta\bar{p}$	$-\frac{1}{2}c^2\kappa_\varepsilon^2\{J_1^2(\lambda_1\bar{r}) + \lambda_1^2\bar{z}^2[J_0^2(\lambda_1\bar{r}) + J_1^2(\lambda_1\bar{r})]\}$
	Beltramian case with slip
$\bar{u}_\theta$	$\frac{1}{\bar{r}}\sqrt{1+c^2\lambda_1^2\kappa_\varepsilon^2\bar{r}^2\bar{z}^2J_1^2\,(\lambda_1\bar{r})}$
$\bar{\boldsymbol{\omega}}$	$-\dfrac{c^2\lambda_1^2\kappa_\varepsilon^2\bar{r}\bar{z}J_1^2\,(\lambda_1\bar{r})}{\sqrt{1+c^2\lambda_1^2\kappa_\varepsilon^2\bar{r}^2\bar{z}^2J_1^2\,(\lambda_1\bar{r})}}\boldsymbol{e}_r + c\lambda_1^2\kappa_\varepsilon\bar{z}J_1\,(\lambda_1\bar{r})\,\boldsymbol{e}_\theta + \dfrac{c^2\lambda_1^3\kappa_\varepsilon^2\bar{r}\bar{z}^2J_0\,(\lambda_1\bar{r})\,J_1\,(\lambda_1\bar{r})}{\sqrt{1+c^2\lambda_1^2\kappa_\varepsilon^2\bar{r}^2\bar{z}^2J_1^2\,(\lambda_1\bar{r})}}\boldsymbol{e}_z$
$\dfrac{\partial \bar{p}}{\partial \bar{r}}$	$\bar{r}^{-3} + c^2\kappa_\varepsilon^2\left[(1+\lambda_1^2\bar{z}^2)\bar{r}^{-1}J_1^2(\lambda_1\bar{r}) - \lambda_1 J_1(\lambda_1\bar{r})J_0(\lambda_1\bar{r})\right]$
$\Delta\bar{p}$	$-\frac{1}{2}\bar{r}^{-2} - \frac{1}{2}c^2\kappa_\varepsilon^2\{J_1^2(\lambda_1\bar{r}) + \lambda_1^2\bar{z}^2[J_0^2(\lambda_1\bar{r}) + J_1^2(\lambda_1\bar{r})]\} + \frac{1}{2}$

and maxima, mantle location, crossflow velocity, pressure distributions, pressure gradients, vorticity, and swirl intensity. The main advantage of the new helical solutions may be connected to their swirl velocity exhibiting a physically realizable axial dependence, to their non-zero vorticity in all three spatial directions, to the parallelism between their velocities and vorticities, and to their alternate mantle location, which seems to not only agree with but also complement existing sets of reported simulations and experimental measurements. Some of these reports suggest that mantle positioning can be influenced by the shape, size, and placement of the outlet section or so-called vortex finder. For this reason, an effort to characterize the impact of the chamber's exit opening on the flow has been carried out based on the extended solution with sidewall injection. For each family of solutions developed here, we have attempted to either impose or relax the no-slip requirement at the sidewall. This has led to two classes of self-similar solutions with dissimilar attributes. The first, no-slip preserving motions are found to not only vanish at the sidewall, but also along the centreline where a forced vortex region is invariably formed. This configuration results in the theoretical Trkalian profiles with tangential speeds that vanish both at the centreline and along the chamber wall. Furthermore, all three components of the Trkalian velocity vector appear at the same order. The second, slip permitting profiles are substantially dominated by the free vortex motion that emerges from their analysis. Consequently, their

Table 6. Beltramian and Trkalian cases with sidewall injection and $\upsilon = \frac{1}{2}\pi/L$.

Variable	Equation
	Common parts
$\bar{\psi}$	$c\kappa_\varepsilon l\,\bar{r}\sin\left(\frac{1}{2}\pi\bar{z}/l\right)J_1(\lambda_1\bar{r})$
$\bar{u}_r$	$-\frac{1}{2}\pi c\kappa_\varepsilon\cos\left(\frac{1}{2}\pi\bar{z}/l\right)J_1(\lambda_1\bar{r})$
$\bar{u}_z$	$c\lambda_1\kappa_\varepsilon l\sin\left(\frac{1}{2}\pi\bar{z}/l\right)J_0(\lambda_1\bar{r})$
$\dfrac{\partial\bar{p}}{\partial\bar{z}}$	$-\frac{1}{4}\pi c^2\lambda_1^2\kappa_\varepsilon^2 l[J_0^2(\lambda_1\bar{r})+J_1^2(\lambda_1\bar{r})]\sin(\pi\bar{z}/l)$
	Trkalian case with no slip
$\bar{u}_\theta$	$\frac{1}{2}\pi c\kappa_\varepsilon\sqrt{1+4\lambda_1^2 l^2/\pi^2}\sin\left(\frac{1}{2}\pi\bar{z}/l\right)J_1(\lambda_1\bar{r})$
$\bar{\boldsymbol{\omega}}$	$\begin{cases}-\frac{1}{2}c\pi\kappa_\varepsilon\sqrt{\lambda_1^2+\frac{1}{4}\pi^2/l^2}J_1(\lambda_1\bar{r})\cos\left(\frac{1}{2}\pi\bar{z}/l\right)\boldsymbol{e}_r+c\kappa_\varepsilon l(\lambda_1^2+\frac{1}{4}\pi^2/l^2)J_1(\lambda_1\bar{r})\sin\left(\frac{1}{2}\pi\bar{z}/l\right)\boldsymbol{e}_\theta\\ +c\kappa_\varepsilon l\lambda_1\sqrt{\lambda_1^2+\frac{1}{4}\pi^2/l^2}J_0(\lambda_1\bar{r})\sin\left(\frac{1}{2}\pi\bar{z}/l\right)\boldsymbol{e}_z\end{cases}$
$\dfrac{\partial\bar{p}}{\partial\bar{r}}$	$\frac{1}{4}c^2\kappa_\varepsilon^2 J_1(\lambda_1\bar{r})\left\{-\pi^2\lambda_1 J_0(\lambda_1\bar{r})+\bar{r}^{-1}J_1(\lambda_1\bar{r})\left[\pi^2+2l^2\lambda_1^2-2l^2\lambda_1^2\cos(\pi\bar{z}/l)\right]\right\}$
$\Delta\bar{p}$	$-\frac{1}{8}c^2\kappa_\varepsilon^2\left\{\pi^2 J_1^2(\lambda_1\bar{r})+2\lambda_1^2 l^2[J_0^2(\lambda_1\bar{r})+J_1^2(\lambda_1\bar{r})][1-\cos(\pi\bar{z}/l)]\right\}$
	Beltramian case with slip
$\bar{u}_\theta$	$\frac{1}{\bar{r}}\sqrt{1+c^2\kappa_\varepsilon^2\left(\lambda_1^2 l^2+\frac{1}{4}\pi^2\right)\bar{r}^2 J_1^2(\lambda_1\bar{r})\sin^2\left(\frac{1}{2}\pi\bar{z}/l\right)}$
$\bar{\boldsymbol{\omega}}$	$\begin{cases}-\dfrac{c^2\pi\kappa_\varepsilon^2(\pi^2+4l^2\lambda_1^2)\bar{r}J_1^2(\lambda_1\bar{r})\sin(\pi\bar{z}/l)}{8l\sqrt{4+c^2\kappa_\varepsilon^2(\pi^2+4l^2\lambda_1^2)\bar{r}^2 J_1^2(\lambda_1\bar{r})\sin^2\left(\frac{1}{2}\pi\bar{z}/l\right)}}\boldsymbol{e}_r+\dfrac{c\kappa_\varepsilon}{4l}(\pi^2+4l^2\lambda_1^2)J_1(\lambda_1\bar{r})\sin\left(\frac{1}{2}\pi\bar{z}/l\right)\boldsymbol{e}_\theta\\ +\dfrac{c^2\lambda_1\kappa_\varepsilon^2(\pi^2+4l^2\lambda_1^2)\bar{r}J_0(\lambda_1\bar{r})J_1(\lambda_1\bar{r})[1-\cos(\pi\bar{z}/l)]}{4\sqrt{4+c^2\kappa_\varepsilon^2(\pi^2+4l^2\lambda_1^2)\bar{r}^2 J_1^2(\lambda_1\bar{r})\sin^2\left(\frac{1}{2}\pi\bar{z}/l\right)}}\boldsymbol{e}_z\end{cases}$
$\dfrac{\partial\bar{p}}{\partial\bar{r}}$	$\bar{r}^{-3}+\frac{1}{4}c^2\kappa_\varepsilon^2 J_1(\lambda_1\bar{r})\left\{-\pi^2\lambda_1 J_0(\lambda_1\bar{r})+\bar{r}^{-1}J_1(\lambda_1\bar{r})\left[\pi^2+2l^2\lambda_1^2-2l^2\lambda_1^2\cos(\pi\bar{z}/l)\right]\right\}$
$\Delta\bar{p}$	$-\frac{1}{2}\bar{r}^{-2}-\frac{1}{8}c^2\kappa_\varepsilon^2\left\{\pi^2 J_1^2(\lambda_1\bar{r})+2\lambda_1^2 l^2[J_0^2(\lambda_1\bar{r})+J_1^2(\lambda_1\bar{r})][1-\cos(\pi\bar{z}/l)]\right\}+\frac{1}{2}$

tangential speeds exceed their axial and radial velocity contributions proportionately with the product of the swirl number and the chamber aspect ratio. These lead to axially linear and nonlinear Beltramian flow fields with identical radial pressure gradients and pressure variations when compared to one another and to the former, complex lamellar profile obtained by Vyas and Majdalani (2006). Much like the boundary layer treatment of the complex lamellar solution by Majdalani and Chiaverini (2009), the Beltramian solutions require a detailed asymptotic analysis to suppress their core and wall singularities. Nonetheless, being derived directly from the BHE, the new set of Beltramian motions increase our repertoire of exact inviscid solutions for bidirectional helical flows in cyclonic chambers.

In closing, it may be instructive to remark that, throughout this work, the Beltramian profiles are considered first with no sidewall injection, with the aim of simulating the bulk gaseous motion in cyclonic separators and VCCWC thrust chambers. The analysis is then repeated for the case comprising sidewall injection, which can be used to model the average mean flow in vortex-dominated hybrid propellant VIHRE chambers. In practice, the resulting expressions enable us to mimic the effects of wall blowing on the basic flow properties, mantle location, peak velocities and pressures, etc. Along similar lines, they allow us to evaluate the effects of varying the outlet fraction in the exit plane, a geometric property that has been connected, in some applications at least, with the relative sizes of vortex finders and nozzle diameters. In the wall-blowing configuration, for instance, our eigenvalues are computed as function of the chamber outlet fraction β, sidewall injection ratio ε, and tangential inflow parameter κ. The latter gauges the relative order of the off-swirl components, thus signaling the onset of a swirl-intensive motion with successive decreases in magnitude. This Ekman-like number may also pose as a small perturbation parameter, which can be suitably employed in later extensions of this work, where the present models may serve as outer far-field approximations. Finally, the partial solutions obtained with sidewall injection are categorically found to depend on an effective inflow parameter, $\kappa_\varepsilon \equiv \kappa + \varepsilon$. This dimensionless grouping proves to be a linear combination of its impermeable counterpart and the sidewall injection ratio. In forthcoming analysis, the helical models introduced here will be used at the basis of a full-scale stability study of cyclonic motions, where the availability of a mean flow remains vital. It can therefore be seen that these basic flow profiles may open up new lines of research inquiry, such as the ability to investigate the impact of swirl on vortex coherence and breakdown. They may also permit the development of multidimensional mathematical strategies that can be suitably applied to the treatment of viscous boundary layers in cyclonic chambers, and of flow compressibility caused by high speed injection.

Acknowledgments

This material is based on work supported partly by the National Science Foundation, and partly by the H H Arnold Chair of Excellence in Advanced Propulsion, the University of Tennessee Space Institute.

References

Anderson M H, Valenzuela R, Rom C J, Bonazza R and Chiaverini M J 2003 Vortex chamber flow field characterization for gelled propellant combustor applications *AIAA Paper* 2003–4474

Aris R 1962 *Vectors, Tensors and the Basic Equations of Fluid Mechanics* (Mineala, NY: Dover)

Barber T A and Majdalani J 2009 Exact Eulerian solution of the conical bidirectional vortex *AIAA Paper* 2009–5306

Batchelor G K 1967 *An Introduction to Fluid Dynamics* (Cambridge: Cambridge University Press)

Batterson J W and Majdalani J 2010 Sidewall boundary layers of the bidirectional vortex *J. Propul. Power* **26** 102–12

Bloor M I G and Ingham D B 1973 Theoretical investigation of the flow in a conical hydrocyclone *Trans. Inst. Chem. Eng.* **51** 36–41

Bloor M I G and Ingham D B 1987 The flow in industrial cyclones *J. Fluid Mech.* **178** 507–19

Bragg S L and Hawthorne W R 1950 Some exact solutions of the flow through annular cascade actuator disks *J. Aerospace Sci.* **17** 243–9

Chang F and Dhir V K 1995 Mechanisms of heat transfer enhancement and slow decay of swirl in tubes using tangential injection *Int. J. Heat Fluid Flow* **16** 78–87

Chiaverini M J, Malecki M J, Sauer J A, Knuth W H and Majdalani J 2003 Vortex thrust chamber testing and analysis for O_2–H_2 propulsion applications *AIAA Paper* 2003–4473

Cortes C and Gil A 2007 Modeling the gas and particle flow inside cyclone separators *Prog. Energy Combust. Sci.* **33** 409–52

Derksen J and van den Akker H 2000 Simulation of vortex core precession in a reverse-flow cyclone *AICHE J.* **46** 1317–31

Fang D, Majdalani J and Chiaverini M J 2003 Simulation of the cold-wall swirl driven combustion chamber *AIAA Paper* 2003–5055

Fang D, Majdalani J and Chiaverini M J 2004 Hot flow model of the vortex cold wall liquid rocket *AIAA Paper* 2004–3676

Fontein F J and Dijksman C 1953 *Recent Developments in Mineral Dressing* (London: Institution of Mining and Metallurgy)

Gloyer P W, Knuth W H and Goodman J 1993 Overview of initial research into the effects of strong vortex flow on hybrid rocket combustion and performance *CSTAR Fifth Annual Symposium Paper* N96-16953

Hill M 1894 On a spherical vortex *Phil. Trans. R. Soc. A* **185** 213–45

Hoekstra A J, Derksen J J and van den Akker H E A 1999 An experimental and numerical study of turbulent swirling flow in gas cyclones *Chem. Eng. Sci.* **54** 2055–65

Hoekstra A J, van Vliet E, Derksen J J and van den Akker H E A 1998 Vortex core precession in a gas cyclone *Advances in Turbulence* VII ed U Frisch (Dordrecht: Kluwer)

Hsieh K and Rajamani R 1991 Mathematical model of the hydrocyclone based on physics of fluid flow *AICHE J.* **37** 735–46

Hu L, Zhou L, Zhang J and Shi M 2005 Studies of strongly swirling flows in the full space of a volute cyclone separator *AICHE J.* **51** 740–9

Kelsall D 1952 A study of the motion of solid particles in a hydraulic cyclone *Trans. Inst. Chem. Eng.* **30** 87–103

Kirshner R P 2004 *The Extravagant Universe: Exploding Stars, Dark Energy, and the Accelerating Cosmos* (Princeton, NJ: Princeton University Press)

Knuth W H, Bemowski P A, Gramer D J, Majdalani J and Rothbauer W J 1996 Gas-fed, vortex injection hybrid rocket engine *SBIR Phase I Final Technical Report* NASA/MSFC Contract NAS8-40679, NASA Marshall Space Flight Center, Huntsville, AL

Königl A 1986 Stellar and galactic jets: theoretical issues *Can. J. Phys.* **64** 362–8

Maicke B and Majdalani J 2009 A constant shear stress core flow model of the bidirectional vortex *Proc. R. Soc. Lond.* A **465** 915–35

Majdalani J 2007 Vortex injection hybrid rockets *Fundamentals of Hybrid Rocket Combustion and Propulsion AIAA Progress in Astronautics and Aeronautics* ed K Kuo and M J Chiaverini (Washington, DC: AIAA) pp 247–76

Majdalani J and Chiaverini M J 2009 On steady rotational cyclonic flows: the viscous bidirectional vortex *Phys. Fluids* **21** 103603–15

Majdalani J and Rienstra S 2007 On the bidirectional vortex and other similarity solutions in spherical coordinates *J. Appl. Math. Phys. (ZAMP)* **58** 289–308

Majdalani J and Saad T 2007 The Taylor–Culick profile with arbitrary headwall injection *Phys. Fluids* **19** 093601–10

Matveev I, Matveeva S and Serbin S 2007 Design and preliminary test results of the plasma assisted tornado combustor *AIAA Paper* 2007-5628

Molina R, Wang S, Gomez L, Mohan R, Shoham O and Kouba G 2008 Wet gas separation in gas–liquid cylindrical cyclone separator *J. Energy Resources Technol.* **130** 042701–13

Murray A L, Gudgen A J, Chiaverini M J, Sauer J A and Knuth W H 2004 Numerical code development for simulating gel propellant combustion processes *JANNAF Paper* 2004–0115

Penner S 1972 Elementary considerations of the fluid mechanics of tornadoes and hurricanes *Acta Astron.* **17** 351–62

Reydon R and Gauvin W 1981 Theoretical and experimental studies of confined vortex flow *Canad. J. Chem. Eng.* **59** 14–23

Rom C J, Anderson M H and Chiaverini M J 2004 Cold flow analysis of a vortex chamber engine for gelled propellant combustor applications *AIAA Paper* 2004-3359

Smith J 1962a An analysis of the vortex flow in the cyclone separator *ASME J. Basic Eng.* **84** 609–18

Smith J 1962b An experimental study of the vortex in the cyclone separator *ASME J. Basic Eng.* **84** 602–8

ter Linden A 1949 Investigations into cyclone dust collectors *Proc. Inst. Mech. Eng.* **160** 233–51

Truesdell C 1954 *The Kinematics of Vorticity* (Bloomington, IN: Indiana University Press)

Vatistas G, Jawarneh A and Hong H 2005 Flow characteristics in a vortex chamber *Can. J. Chem. Eng.* **83** 425–36

Vatistas G, Lin S and Kwok C 1986a Reverse flow radius in vortex chambers *AIAA J.* **24** 1872–3

Vatistas G, Lin S and Kwok C 1986b Theoretical and experimental studies on vortex chamber flows *AIAA J.* **24** 635–42

Vyas A and Majdalani J 2006 Exact solution of the bidirectional vortex *AIAA J.* **44** 2208–16

Wu J Z, Ma H Y and Zhou M D 2006 *Vorticity and Vortex Dynamics* (New York: Springer)

Zhiping Z, Yongjie N and Qinggang L 2008 Pressure drop in cyclone separator at high pressure *J. Therm. Sci.* **17** 275–80